



AFRL-RH-WP-TR-2010-0141

**Radio Frequency Controlled Stimulation of
Intracellular Gold or Silver Nanoparticle
Conjugates for Use as Potential Sensors
Or Modulators of Biological Function**

**Richard C. Murdock
Saber M. Hussain
Biosciences and Protection Division
Applied Biotechnology Branch**

September 2010

Interim Report for July 2010 – August 2010

**Distribution A: Approved for public release;
distribution unlimited.**

**Air Force Research Laboratory
711 Human Performance Wing
Human Effectiveness Directorate
711th Human Performance Wing
Biosciences and Protection Division
Applied Biotechnology Branch**

NOTICE

Using Government drawings, specifications, or other data included in this document for any purpose other than Government procurement does not in any way obligate the U.S. Government. The fact that the Government formulated or supplied the drawings, specifications, or other data does not license the holder or any other person or corporation; or convey any rights or permission to manufacture, use, or sell any patented invention that may relate to them.

This report was cleared for public release by the 88th Air Base Wing Public Affairs Office and is available to the general public, including foreign nationals. Copies may be obtained from the Defense Technical Information Center (DTIC) (<http://www.dtic.mil>).

AFRL-RH-WP-TR-2010-0141

THIS REPORT HAS BEEN REVIEWED AND IS APPROVED FOR PUBLICATION IN
ACCORDANCE WITH ASSIGNED DISTRIBUTION STATEMENT.

//SIGNED//

DAVID R. MATTIE, PhD, DR-III
Work Unit Manager
Applied Biotechnology Branch

//SIGNED//

MARK M. HOFFMAN, Deputy Chief
Biosciences and Protection Division
Human Effectiveness Directorate
711th Human Performance Wing
Air Force Research Laboratory

This report is published in the interest of scientific and technical information exchange, and its publication does not constitute the Government's approval or disapproval of its ideas or findings.

REPORT DOCUMENTATION PAGE				Form Approved OMB No. 0704-0188	
Public reporting burden for this collection of information is estimated to average 1 hour per response, including the time for reviewing instructions, searching existing data sources, gathering and maintaining the data needed, and completing and reviewing this collection of information. Send comments regarding this burden estimate or any other aspect of this collection of information, including suggestions for reducing this burden to Department of Defense, Washington Headquarters Services, Directorate for Information Operations and Reports (0704-0188), 1215 Jefferson Davis Highway, Suite 1204, Arlington, VA 22202-4302. Respondents should be aware that notwithstanding any other provision of law, no person shall be subject to any penalty for failing to comply with a collection of information if it does not display a currently valid OMB control number. PLEASE DO NOT RETURN YOUR FORM TO THE ABOVE ADDRESS.					
1. REPORT DATE (DD-MM-YYYY) September 2010		2. REPORT TYPE Interim Report		3. DATES COVERED (From - To) Jul 10 – Aug 10	
4. TITLE AND SUBTITLE Radio Frequency Controlled Stimulation of Intracellular Gold or Silver Nanoparticle Conjugates for Use as Potential Sensors or Modulators or Biological Function				5a. CONTRACT NUMBER	
				5b. GRANT NUMBER NA	
				5c. PROGRAM ELEMENT NUMBER 62202F	
6. AUTHOR(S) Richard C. Murdock; Saber M. Hussain				5d. PROJECT NUMBER 7184	
				5e. TASK NUMBER D4	
				5f. WORK UNIT NUMBER 7184D410	
7. PERFORMING ORGANIZATION NAME(S) AND ADDRESS(ES) 711 HPW/RHPB; 2729 R Street, Wright-Patterson AFB OH 45433-5707				8. PERFORMING ORGANIZATION REPORT NUMBER	
9. SPONSORING / MONITORING AGENCY NAME(S) AND ADDRESS(ES) Air Force Materiel Command Air Force Research Laboratory 711th Human Performance Wing Human Effectiveness Directorate Biosciences and Protection Division Applied Biotechnology Branch Wright-Patterson AFB OH 45433-5707				10. SPONSOR/MONITOR'S ACRONYM(S) 711 HPW/RHPB	
				11. SPONSOR/MONITOR'S REPORT NUMBER(S) AFRL-RH-WP-TR-2010-0141	
12. DISTRIBUTION / AVAILABILITY STATEMENT Distribution A: Approved for public release; distribution unlimited.					
13. SUPPLEMENTARY NOTES 88ABW cleared 7 January 2011, 88ABW-2010-6669					
14. ABSTRACT The objective of this investigation was to explore the ability of a radio frequency (RF) signal to interact with metal nanoparticles for the purposes of remote stimulation or control of cellular processes. For this study, spherical gold nanoparticles (Au NPs, 4nm and 13 nm) and spherical silver nanoparticles (Ag NPs, 8nm) were synthesized, biofunctionalized with oligonucleotides, and hybridized through the oligonucleotide functionalization as a potential method of intracellular control. Initial Au and Ag NP heating studies showed significant heating of unfunctionalized Au and Ag NPs of greater than 40° C in less than 180 seconds. Biofunctionalized Au and Ag NPs showed significantly less heat transfer to solution, indicating most heat transfer was absorbed by oligonucleotide. Biocompatibility assessment studies were also conducted on the unfunctionalized and functionalized Au and Ag NPs and did not show significant impact on cell viability after 24 hours. These results demonstrate that Au and Ag NPs show promising potential for sensing applications using remote RF control.					
15. SUBJECT TERMS Radio frequency signal nanoparticles biofunctionalized oligonucleotides					
16. SECURITY CLASSIFICATION OF:			17. LIMITATION OF ABSTRACT	18. NUMBER OF PAGES	19a. NAME OF RESPONSIBLE PERSON
a. REPORT	b. ABSTRACT	c. THIS PAGE			David R. Mattie
U	U	U	SAR	72	19b. TELEPHONE NUMBER (include area code) NA

THIS PAGE INTENTIONALLY LEFT BLANK.

ABSTRACT

The objective of this investigation was to explore the ability of a radio frequency (RF) signal to interact with metal nanoparticles for the purposes of remote stimulation or control of cellular processes. For this study, spherical gold nanoparticles (Au NPs, 4 nm and 13 nm) and spherical silver nanoparticles (Ag NPs, 8nm) were synthesized, biofunctionalized with oligonucleotides, and hybridized through the oligonucleotide functionalization as a potential method of intracellular control. Initial Au and Ag NP heating studies showed significant heating of unfunctionalized Au and Ag NPs of greater than 40°C in less than 180 seconds. Biofunctionalized Au and Ag NPs showed significantly less heat transfer to solution, indicating most heat transfer was absorbed by oligonucleotide. Biocompatibility assessment studies were also conducted on the unfunctionalized and functionalized Au and Ag NPs and did not show significant impact on cell viability after 24 hours. These results demonstrate that Au and Ag NPs show promising potential for sensing applications using remote RF control.

TABLE OF CONTENTS

<u>Section</u>	<u>Page</u>
List of Figures	iv
List of Tables	v
Preface.....	vi
Acknowledgments.....	vii
I. Summary	1
II. Introduction.....	2
a. Background	3
i. Colloidal Gold and Silver	3
ii. Radio Frequency Heating of Nanomaterials	4
b. Experimental Approach	6
III. Nanomaterial Synthesis	8
a. Materials and Methods.....	8
i. Synthesis of Gold and Silver Colloids	8
ii. Characterization of Gold and Silver Colloids	9
b. Results	10
c. Discussion	17
IV. Functionalization of Nanomaterials	19
a. Materials and Methods.....	19
i. Functionalization of Gold and Silver Colloids	19
ii. Characterization of Functionalized Gold and Silver Colloids	22
b. Results	23
c. Discussion	31
V. Biocompatibility of Nanomaterials	34
a. Materials and Methods.....	34
i. Cell Culture	34
ii. Biocompatibility Assessments	34
b. Results	36
c. Discussion	43
VI. Radio Frequency Heating of Nanomaterials	45
a. Materials and Methods.....	45
i. Radio Frequency Exposure System	45
b. Results	45
c. Discussion	49
VII. Conclusions and Future Work	50
VIII. References	52
IX. Appendices.....	59
List of Acronyms, Abbreviations, and Symbols	61

LIST OF FIGURES

Figure 1. Representative Scale Comparison for Nanomaterials	2
Figure 2. Applications of RF Heating of Biofunctionalized Nanomaterials	7
Figure 3. 13 nm Au Colloid Synthesis.....	11
Figure 4. 4 nm Au Colloid Synthesis.....	12
Figure 5. 8 nm Ag Colloid Synthesis.....	13
Figure 6. UV-Vis Absorption Spectra of 13 nm Au Colloid Batch 3.....	15
Figure 7. UV-Vis Absorption Spectra of 4 nm Au Colloid Batches 2, 3, 4, and 5.....	16
Figure 8. UV-Vis Absorption Spectra of Ag Colloid Batches 1, 2, 4, 5, and 6.....	17
Figure 9. Diagram of Functionalization Procedure.....	22
Figure 10. Functionalized and Hybridized 13 nm Au NPs.....	24
Figure 11. Hybridized Ag and Au NPs.....	25
Figure 12. UV-Vis Absorption Spectra of Unfunctionalized and Functionalized Au and Ag NPs	27
Figure 13. Dehybridization Curves for Hybridized 13 nm Au NPs	28
Figure 14. Functionalized and Hybridized 4 nm Au and 8 nm Ag NPs	29
Figure 15. Functionalized and Hybridized 4 nm Au and 8 nm Ag NPs	30
Figure 16. Hyperspectral Imaging of Unfunctionalized, Functionalized, and Hybridized Au NPs.....	31
Figure 17. Biocompatibility of Unfunctionalized 4 nm Au NPs and 8 nm Ag NPs in HaCaT cells.....	37
Figure 18. Biocompatibility of Unfunctionalized, Functionalized, and Hybridized 13 nm Au NPs in PC-12 Cells	38
Figure 19. Biocompatibility of Unfunctionalized 4 nm Au NPs and 8 nm Ag NPs in PC-12 Cells	39
Figure 20. CytoViva URI Images of HaCaT Cells and PC-12 Cells Treated with Unfunctionalized 4 nm Au and 8 nm Ag NPs	40
Figure 21. Uptake of Unfunctionalized 4 nm Au NPs into HaCaT Cells.....	41
Figure 22. Uptake of Unfunctionalized 4 nm Au NPs into HaCaT Cells.....	42
Figure 23. Hyperspectral Imaging of Untreated HaCaT Cells and HaCaT Cells Treated with Hybridized 13 nm Au NPs.....	43
Figure 24. RF Heating Curves of Unfunctionalized Au and Ag NPs in Water and Hybridization Buffer	46
Figure 25. RF Heating Curves of Unfunctionalized, Functionalized, and Hybridized Au and Ag NPs	48

LIST OF TABLES

Table 1. Dynamic Light Scattering (DLS) and Laser Doppler Velocimetry (LDV) Results for Various Batches of Synthesized Colloids.....	14
Table 2. Dynamic Light Scattering (DLS) Results for Unfunctionalized, Functionalized, and Hybridized 13 nm Au NPs	26
Table 3. Differences in NP Sample Physical Characteristics When Dispersed at Equal Total Volume Concentrations	47
Table 4. Power Output Calculations With Respect to Number of Particles, Particle Surface Area, and Particle Volume	49

PREFACE

This research work was conducted as partial fulfillment of a Master of Science degree and presented as a thesis project by the first author. The academic affiliation for this project was through the Biomedical, Industrial, and Human Factors Engineering Department at Wright State University in Fairborn, OH. The project was supported through an Air Force Research Laboratory (AFRL) Human Effectiveness Directorate (711 HPW/RH) Chief Scientist Seedling program. The first author was supported partially by an appointment to the Student Research Participation Program at AFRL, administered by the Oak Ridge Institute for Science and Education through an interagency agreement between the U.S. Department of Energy and AFRL, and partially through the Student Career Enhancement Program, administered by the U.S. Office of Personnel Management.

ACKNOWLEDGEMENTS

The authors would like to graciously acknowledge Dr. John Schalger, 711 HPW/RHPB Branch Chief, Dr. Morley Stone, AFRL/711 HPW/RH Chief Scientist, and Col. Patricia Reilly, 711 HPW RH Division Chief who supported, provided seedling funding, and allowed the project to be performed in the Air Force Research Laboratories. The authors would like to specially recognize Dr. David Reynolds, BME department at WSU, for his help and mentorship of this research. The authors would like to thank Dr. Jorge Chavez-Beneviedes, 711 HPW/RHPC, for his knowledge of nanomaterial functionalization and help with the process. The authors would also like to specially thank Dr. Zach Hilt, Chemical Engineering Department, University of Kentucky, and his graduate students Nitin Satarkar and Churn Poh, for allowing the use of their RF system for these studies and being very hospitable and accommodating.

SUMMARY

The objective of this investigation was to explore the ability of a radio frequency (RF) signal to interact with metal nanoparticles (NPs) for the purposes of remote stimulation or control of cellular processes. Gold (Au) NPs, as well as other noble metal NPs, have been shown in literature to be remotely heated with exposure to RF signals. However, in these studies, the heating of the nanomaterials (NMs) was constant and uncontrolled. For this study, it is expected that by better understanding the RF heating characteristics of these materials and its impact on surface functionalizations, a remotely stimulated control mechanism can be developed at the nanoscale, with applications in the control of cellular signaling. Spherical Au NPs (4 nm and 13 nm) and spherical silver (Ag) NPs, 8 nm) were synthesized, biofunctionalized with oligonucleotides, and hybridized through the oligonucleotide functionalization as a potential method of intracellular control. Full characterization of the NPs post-synthesis, post-functionalization, and post-hybridization was performed. Biocompatibility assessment studies were also conducted on the unfunctionalized and functionalized Au and Ag NPs and did not show any significant impact on cell viability after 24 hours. Also, initial Au and Ag NP heating studies were conducted by exposure to a 13.56 MHz RF frequency at 400W power output for 180 seconds and sample solution temperature was measured via infrared thermal imaging. Unfunctionalized Au and Ag NPs were tested with all samples showing significant heating of greater than 40°C. Biofunctionalized Au and Ag NPs showed significantly less heat transfer to solution, indicating most heat transfer was absorbed by the oligonucleotides. These results show that Au and Ag NPs can be useful for remote RF control of biomolecules attached to the surface without transferring potentially detrimental heat to the surrounding environment. This means the particles could be used *in vitro* or potentially *in vivo* without negative impacts to the host.

INTRODUCTION

Nanomaterials (NMs), by definition, have one dimension that falls into the 1-100 nm range, with the NMs typically being comprised of metals, metal oxides, silica, or carbon¹. To give a perspective of the size scale difference between our normal reference scale and the nano-scale, if a 30 nm nanoparticle (NP) was compared to a meter stick, the meter stick would need to be the size of the earth just to make the NP the size of a ping pong ball. Figure 1 gives a comparison of the size disparity described here². At the nano-scale, materials can have unique physicochemical properties which their bulk counterparts do not possess. Therefore, the convergence of biological systems and nanotechnology has led to the development of unique nanostructures that incorporate the highly selective catalytic and recognition properties of natural materials, such as proteins/enzymes and DNA, with the unique electronic, photonic, and catalytic features of NMs. In medicine, proposed uses for NMs such as nanotubes, nanowires, fullerene derivatives (buckyballs) and quantum dots are currently used for imaging, sensing, and targeted gene and drug delivery³⁻⁶.

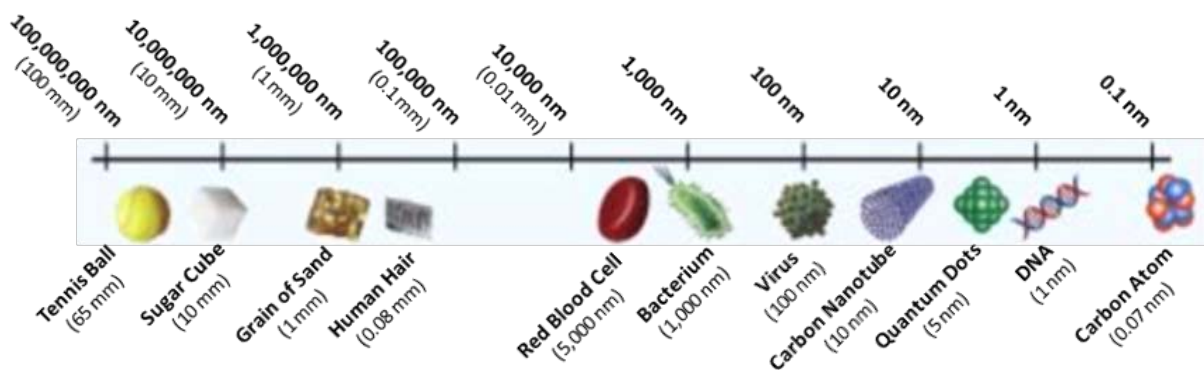


Figure 1. Representative Scale Comparison for Nanomaterials.

Bionanomaterials have been developed that have novel physical/chemical properties and functions due to their advantageous, miniscule size. In particular, NPs are now used to target synthetic peptides, proteins, oligonucleotides and plasmids to specific cell types while protecting these macromolecules from enzymatic degradation^{7,8}. In addition, NPs have been proposed for the treatment of many diseases which require a constant drug concentration in the blood, or drug targeting to specific cells or organs^{9,10}. Also, NPs can be utilized to treat diseases that require a sustained presentation of the drug at several anatomical sites^{10,11}. Furthermore, companies in the food and cosmetics industries have incorporated NMs to enhance the quality of their products¹². Lastly, defense and engineering scientists have shown that NMs are potentially useful in electronics, sensors, munitions, and energetic/reactive systems involved with the advancement of propulsion technology¹³.

Background

Colloidal Gold and Silver Nanoparticles. Gold nanoparticles (Au NPs), or colloids, have been used for cell imaging, targeted drug delivery, cancer diagnostics and medical therapeutic applications¹⁴⁻¹⁷. This is mainly due to the ease of functionalization with

biomolecules through the thiol linkage. This thiol bond with the Au NP surface has nearly the strength of a disulfide bond¹⁸, and one or two Au atoms on the surface of the NP can interact with any one sulfur molecule, making the bond extremely stable^{18,19}. Au NPs also serve as a model system for NP studies and products due to their large, producible size range, and large shape range with 1:1 to 1:5 aspect ratios possible. Traditionally, these NPs have been considered non-toxic^{20,21}; however, studies have shown that Au NPs can display toxicity based on factors such as size, charge, and surface modifications²²⁻²⁵.

Silver nanoparticles (Ag NPs) currently have a variety of uses in everyday consumers' lives such as nanosilver infused storage containers, nanosilver coated surfaces of medical devices to reduce hospital related infections, bandages, footwear and countless household items which claim to be anti-microbial²⁶⁻²⁹. Ag NPs have been shown to be effective antimicrobial agents due to their ability to bind to proteins and interfere with bacterial and viral processes^{30,31}. Perhaps one of the most interesting examples is the ability of Ag NPs to bind to HIV-1 and prevent the virus from infecting host cells³². However, Ag NPs have been shown to produce a size and concentration dependent toxicity effect^{33,34}.

The attraction to noble metal NPs, particularly Au and Ag, is the intense local surface plasmon resonance (LSPR or SPR). SPRs are oscillations in the surface electrons of the NPs which cause specific absorption patterns and enhanced reflectance of specific wavelengths in the optical and near infrared regions of the electromagnetic spectrum²⁰. LSPRs are unique to the nano-scale and do not occur in bulk Au and Ag. Both Au and Ag SPRs are sensitive to the NP's surrounding environment, causing a significant shift in the SPR peak when in close proximity to other materials or when molecules interact with the surface of the NPs. For most NPs, the surface is highly reactive since the smaller the particle is, the greater the percentage of atoms comprising the particle are located on the surface which can lead to interactions with material surrounding the NP. This shift in the SPR peak can be measured by observing the changes in the absorption spectrum, i.e. UV-Vis; however, it also correlates to a visible color change in the NP solution, providing a colorimetric response which is recordable by any spectroscopic equipment. Each technique, whether it is absorption or reflection, provides an easy mechanism by which the local state of the NPs can be determined with high sensitivity.

Until recently, Au NPs have been the most widely used for applications involving the use of SPR for colorimetric detection methods due to their previously mentioned ease of synthesis and functionalization. Solutions containing Au NPs in the 10 to 30 nm range typically have a bright crimson red appearance in their normal, well-dispersed condition. However, when aggregated through binding of target molecules or induced through increasing salt concentrations, the solution will turn blue-purple due to the shift of the absorbed and reflected SPR peaks²⁰. Using the SPR measurement of the NPs makes these materials ideal for sensor type applications since no additional tagging, such as fluorescence labeling of the NPs, is needed for tracking or identifying the NP state. However, Ag NPs have approximately 100 times greater light scattering ability than Au NPs, making them even more useful for biosensor applications, since enhanced detection sensitivity can be achieved²⁰.

Currently, there are a plethora of applications involving sensing through functionalized Au or Ag NPs. Chemical sensing using functionalized Au or Ag nanospheres and nanorods has been successful in detecting DNA, heavy metal ions, and immunoproteins, among other targets, at concentrations into the single nano-Molar regime as well as solution pH changes^{20,35-40}. Many of these sensor applications use biomolecules, specifically oligonucleotides, to perform targeted biomolecule capture and provide a concentration dependent, colorimetric response to the binding

event⁴¹⁻⁴³. This linking of oligonucleotides, or short single-stranded DNA, is thermally reversible which allows for a control mechanism of binding. Also, core-satellite assembly of Au and Ag NPs via oligonucleotides showed potential enhancement of SPR effects⁴⁴⁻⁴⁵. Therefore, due to their unique SPR colorimetric response and comparatively facile functionalization procedures, Au and Ag NPs appear to be excellent candidates for this study. Moreover, being conductive materials, they also possess the ability to interact with electromagnetic fields.

Radio Frequency Heating of Nanomaterials. Radio frequency (RF) is a specific range of wavelengths on the electromagnetic spectrum, spanning from 3-300GHz, but typically references the range from about 1 MHz to 1 GHz. Nearly all modern telecommunication modes currently fall into this range. RF is non-ionizing radiation, and studies on the absorption of RF by the body have shown unique frequencies of greater absorption and transmittance. In Bernardi et al. (2003), computer simulation of RF absorption by the body was performed, inputting thermal parameters for 34 different types of tissue, from 10 to 900 MHz. This study showed a maximum absorbance by the body at 40 MHz, a resonance frequency of the body, and a minimum absorption near 300 MHz⁴⁶. This could provide a window of minimal interaction for application of RF to NMs within biological systems.

Au NPs, as well as other noble metal NPs, have been remotely heated with exposure to RF signals. The first applications of this technology were for hyperthermic treatment of cancer cells by continuously heating the Au NPs using a 13.56 MHz RF system until they observed targeted cell death^{47,48}. Fundamentally, the science behind this phenomenon is well known for bulk materials, and appears to coincide at the nano-scale. In alternating current circuits, wires in the circuit will generate heat through resistive losses as the current rapidly switches directions in the wire. As the frequency of the alternating current increases, the current distribution within the wire changes with the current migrating towards the surface of the conductor which is known as the skin effect. Therefore, as the frequency increases, less cross-sectional area of conductor is needed to carry the signal; however, with greater current flow through less area, conductor heating increases also. The area of wire needed to carry a certain frequency signal is known as the skin depth. In electronics, this can be beneficial since it allows less material to be used for the wire carrying the current. With NMs, the RF skin depth is usually greater than the diameter of the NPs being exposed, meaning that the entire volume of the particle is heated. Optimal heating should occur when the skin depth is equal to the diameter of the particle. At the nano-scale, any heating generated in the NP will be transferred nearly immediately to the surrounding environment. If the NP is functionalized with a biomolecule, for example, it will essentially act as a heat sink for the NP. Biomolecules can dissipate heat in less than 50 seconds, allowing for temporary heating of the biomolecules without permanent deformation or denaturing⁴⁹. In Hamad-Schifferli et al. (2002), 1.4 nm Au nanocrystals functionalized with hairpin oligonucleotides were shown to be effectively heated by magnetic field stimulation ($f = 1$ MHz), with reversible control of the dehybridization of the hairpin DNA⁴⁹. The reversing polarity of the magnetic field induces eddy currents within the nanocrystal, which in turn are causing Joule heating of the NP. The theory presented in the paper is that inductive coupling occurs between the oligonucleotide and the NP, allowing the heat to be directly transferred from the particle to the oligonucleotide and reach its dehybridization temperature but not destroy the function of the oligonucleotide⁴⁹. However, in Keblinski et al. (2006), it is suggested that localized heating of NMs is nearly negligible, with only a 0.4 K maximum increase in surface temperature being attained using laser excitation of 65 nm SiO₂-Au NPs⁵⁰. Keblinski and colleagues go on to further analyze magnetic field heating and eddy current heating by RF exposure, concluding that

a surface temperature rise of only 0.1 mK for a 100 nm Au NP and 0.625 μ K for a 50 nm Au NP, respectively⁵⁰. However, when Koblinski et al. analyzed the experiments performed by Hamad-Shifferli et al., they concluded that the DNA temperature increase and subsequent dehybridization must have occurred through other sources or mechanisms since the local induction heating of the 1.7 nm Au NPs would be negligible^{49,50}. They also go on to mention that the DNA molecules used are too large to exhibit selective intramolecular energy distribution through the NP-DNA bond⁵⁰. It appears then that the mechanism, by which the DNA molecules are heating enough to reach their melting temperature, could be simply a local solution heating around the NP. At small NP sizes, under 10 nm in diameter for example, the particle is unable to store any of the heat being generated within the particle. Therefore, the heat that is generated is nearly instantaneously transferred to solution by conduction. However, since the generation of the heat and the immediate transfer to solution is occurring so rapidly, a temperature gradient is set up around the particle as the heat added to solution is faster than the thermal diffusion within the solution. This would provide a region of significantly higher temperatures locally around the particle which could reach the melting temperature of the DNA without the total solution temperature increasing significantly. The evidence presented in both the Hamad-Shifferli paper and the Koblinski paper support this theory^{49,50}.

Additionally, a recent publication by Bendix et al. (2010) experimentally sought out a method by which the local heating of Au NPs exposed to laser sources could be measured⁵¹. In this study, the Au NPs were optically trapped onto a fluorescent lipid bilayer and then exposed to varying power lasers at 532 nm wavelength⁵¹. Bendix and colleagues found that with increasing diameters of the Au NPs, not only does the rate of particle heating increase, but the radius from the NP at which heating is observed increases as well⁵¹. A few other studies of Au NP heating using a capacitively coupled RF system have been conducted, finding significant heating of the NPs in less than one minute of exposure. In Gannon et al. (2008), increasing RF field power (13.56 MHz) and increasing concentrations of 5 nm Au NPs showed increased heating, with the maximum heat transfer to solution occurring at the highest particle concentration and 800 W RF exposure⁵². In Moran et al. (2009), the same capacitively coupled, 13.56 MHz RF system was used to explore differences in Au NP heating rates based on particle size and concentration⁵³. Surprisingly, it was found that the 5 nm, 10 nm, and 250 nm Au nanospheres and 150 nm Au nanoshell particles exhibited the highest heating rates of the samples tested⁵³. This may provide evidence that multiple mechanisms of heating are involved since small and large particles both heated the most. Numerous other experiments involving remote heating of NMs have been performed, mainly through excitation with laser⁵⁴⁻⁵⁷, but a few others using magnetic field excitation^{55,58,59}.

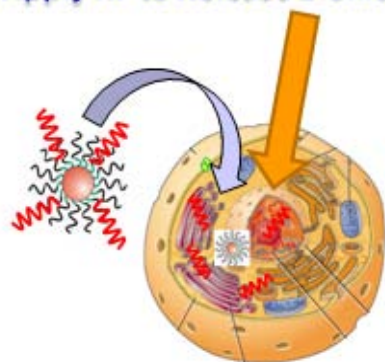
Experimental Approach. The concept of this study was to design a system which allows for external, remote control of, and potentially response detection within, a biological system using biofunctionalized NMs. The specific ability of this technology in the near-term is to be able to control the function of a biomolecule on the surface of a NP, or be able to control the binding state of a NP-biomolecule conjugate. RF heating of noble metal NMs, such as Au, has been previously shown for the use of targeted removal of cancerous cells. It has also been shown that NMs can be functionalized with biomolecules, such as DNA, hybridized together, and controllably heated to dehybridize the NMs. Therefore, it can be hypothesized that noble metal NMs functionalized with DNA, which are formed into a hybridized complex, can be remotely heated and dehybridized upon RF exposure. From these concepts, four specific aims

for this project were established: (1) Synthesize 5-8 nm Au and Ag colloids with minimal size distribution, (2) Functionalize Au and Ag colloids with complimentary oligonucleotides for particle hybridization, (3) Examine the biocompatibility of unfunctionalized and functionalized Au and Ag colloids, and (4) Examine the ability of RF signals to heat unfunctionalized and functionalized Au and Ag colloids.

For this study, a standard size Au NP (13 nm) and 5-8 nm range Au (4 nm) and Ag (8 nm) NPs were synthesized and functionalized with oligonucleotides. This could potentially allow for a remote controlled on/off action to be achieved through heating of the NPs by RF and subsequent control of its surface functionalization and therefore its target. Au and Ag NPs were chosen due to their unique SPR colorimetric response and ability to be inductively heated by RF. Choosing the different sizes not only provided NPs within the range of potential nuclear passivation, but NPs with the greatest potential for heating as deemed from literature. Also, by having two different sizes of Au NPs and one size of Ag NPs, it provided a comparison of RF heating effects of not only different sizes of the same material, but different materials as well. The NPs were functionalized with complementary oligonucleotides and hybridized to form large particle networks. This allowed for a colorimetric detection of the particle hybridization state, and could be used in conjunction with RF exposure to verify dehybridization after heating. Since the ultimate goal of this research effort is to use this control mechanism inside a biological system, biocompatibility of the functionalized particles was assessed to look for any adverse effects of the unfunctionalized, functionalized, and hybridized NPs. The hypothesis was that these functionalized noble metal NPs could passively enter the nucleus and, with proper functionalization, target specific regulatory genes.

The previously described technology would be used to apply targeted, oligonucleotide functionalized, Au NPs to an *in vitro* system which would be exposed to a RF source to disable/enable the targeted biomolecule. Basic research in this area could allow expansion into many different applications in the fields of human performance and intelligence, surveillance, and reconnaissance (ISR). Possible applications for external control include precision disabling of performance detrimental biomolecules and precision delivering of performance enhancing biomolecules (Figure 2). Some remote detection applications are real-time detection of binding events and extremely sensitive real-time detection of very small electromagnetic fields.

Apply RF to Release Biomolecule



Apply RF to Modulate Binding

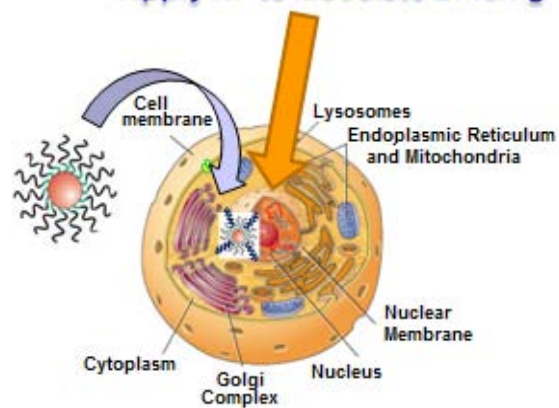


Figure 2. Applications of RF Heating of Biofunctionalized Nanomaterials.

NANOMATERIAL SYNTHESIS

Materials and Methods

Synthesis of 13 nm Gold Colloid. The synthesis of gold colloids in the size range of 10 – 15 nm has been performed in numerous publications. The method described here is an adaptation of the methods cited⁶⁰⁻⁶⁴. In a longneck 1 L round-bottom flask, 500 mL of 0.04% w/v (~0.001 M) gold (III) chloride trihydrate ($\text{HAuCl}_4 \cdot 3\text{H}_2\text{O}$, MW=393.83, MP Biomedicals) was heated to a rapid boil under vigorous stirring on a combination magnetic stirrer – hot plate. Next, 50 mL of 1.14% w/v (~0.0388 M) trisodium citrate dihydrate ($\text{Na}_3\text{C}_6\text{H}_5\text{O}_7 \cdot 2\text{H}_2\text{O}$, MW=294.10, Fluka) was added rapidly to the vortexing solution, resulting in an immediate color change from pale yellow to purple (Figure 3A). The solution was held at boiling and was stirred for an additional 10 min. Approximately 2 min after the start of the 10 min stirring period, the solution slowly changed from purple to a light red color (Figure 3A). The flask was then moved to a non-heated stir plate to continue stirring while the solution was cooled to room temperature. After the solution reached room temperature, it was filtered through a 0.22 μm filter into a brown glass container for storage at room temperature.

Synthesis of 4 nm Gold Colloid. To synthesize the 4 nm Au colloid, stock solutions of 0.4% w/v (~0.01 M) gold (III) chloride trihydrate ($\text{HAuCl}_4 \cdot 3\text{H}_2\text{O}$, MW=393.83, MP Biomedicals), 1.0% w/v (~0.034 M) trisodium citrate dihydrate ($\text{Na}_3\text{C}_6\text{H}_5\text{O}_7 \cdot 2\text{H}_2\text{O}$, MW=294.10, Fluka), and 0.5% w/v (~0.132 M) sodium borohydride (NaBH_4 , MW=37.83, Sigma-Aldrich) were all freshly prepared. The NaBH_4 solution was found to have the greatest impact on the reproducibility of the synthesis process if not freshly prepared. Filtered, autoclaved de-ionized (DI) H_2O (Millipore, resistivity (ρ) = 18.2 $\text{M}\Omega\text{cm}$) was kept at 4°C until ready for use.

The following synthesis process was adapted from literature methods⁶⁵⁻⁶⁸. To begin synthesis, 50 mL of de-ionized H_2O was transferred into a 100 mL glass beaker with a small magnetic stir bar in the bottom. For batch 2, 0.5 mL of 0.4% HAuCl_4 was added to the solution in the beaker and all solutions were at room temperature. For batch 4, 2.5 mL of 0.4% HAuCl_4 was added to the solution in the beaker and all solutions were kept at 4°C. For batches 3 and 5, 1.25 mL of 0.4% HAuCl_4 were added to the solution in the beaker and all solutions were kept at 4°C. Then the beaker was placed on a magnetic stir plate where the solution was mixed vigorously, without splashing of the solution, for approximately 1 min. Next, using a handheld pipette, 500 μL of 0.5% NaBH_4 was added rapidly to the sidewall of the solution while continuing to stir vigorously for 1 min. The solution immediately turned a brown-red color after the addition of the NaBH_4 and then steadily changed to an orange-pink final color. After 1 min, 200 μL of 1.0% $\text{Na}_3\text{C}_6\text{H}_5\text{O}_7$ was added to the solution and continued to stir for another min. Finally, a 5 mL syringe and a 0.22 μm syringe filter were used to filter the final Au colloid solution into a 50 mL centrifuge tube for storage at 4°C.

Synthesis of 8 nm Silver Colloid. To synthesize the 8 nm Ag colloid, stock solutions of 0.4% w/v (~0.024 M) silver nitrate (AgNO_3 , MW=169.87, Sigma-Aldrich), 1.0% w/v (~0.034 M) trisodium citrate dihydrate ($\text{Na}_3\text{C}_6\text{H}_5\text{O}_7 \cdot 2\text{H}_2\text{O}$, MW=294.10, Fluka), and 0.5% w/v (~0.132 M) sodium borohydride (NaBH_4 , MW=37.83, Sigma-Aldrich) were all freshly prepared. The NaBH_4 solution was found to have the greatest impact on the reproducibility of the synthesis

process if not freshly prepared. Filtered, autoclaved DI H₂O ($\rho = 18.2 \text{ M}\Omega\text{cm}$) was kept at 4°C until ready for use.

The following synthesis process was adapted from literature methods⁶⁹. A 100 mL glass beaker was covered with aluminum foil on the sides and top to block light, and a small magnetic stir bar was placed in the bottom. The lights were turned off in the room and dim light from the hallway was used for illumination, except for batch 1 where the room lights were left on. To begin the reaction, 50 mL of the 4°C de-ionized H₂O and 1.25 mL of the 0.4% AgNO₃ were combined in the beaker and then placed on a magnetic stir plate where the solution was mixed vigorously, without splashing of the solution, for approximately 1 min. For batch 3, 500 μL of 100 mM polyethylene glycol (PEG, Hampton Research, MW 400) was added at this point to the stirring solution. Next, using a handheld pipette, 500 μL of 0.5% NaBH₄ was added rapidly to the sidewall of the solution while continuing to stir vigorously for 1 min. The solution immediately turned a black-green color after the addition of the NaBH₄ and then steadily changed to a final color of orange-yellow. For batch 5, 500 μL of 100 mM PEG was added to the stirring solution at this point. After 1 min, 200 μL of 1.0% Na₃C₆H₅O₇ was added to the solution and continued to stir for an additional 1 min. Finally, continuing in the dark, a 5 mL syringe and a 0.22 μm syringe filter were used to filter the final Ag colloid solution into a foil covered 50 mL Falcon centrifuge tube for storage at 4°C.

Characterization of Gold and Silver Colloids

Transmission Electron Microscopy (TEM). Transmission Electron Microscopy (TEM) characterization was performed to obtain the primary particle size and morphology of NPs using a Hitachi H-7600 tungsten-tip instrument at an accelerating voltage of 100 kV in high resolution mode. A TEM uses a high energy electron beam, produced by a filament and focused onto a sample by electromagnetic lenses, to visualize sample features down to tenths of nanometers. Depending on the beam energy, the electrons can penetrate samples below 100 nm in thickness, allowing visualization of the atomic structure for certain samples and crystal structure analysis using diffraction mode settings.

NPs were examined after dilution of NP stock solutions to 100 $\mu\text{g/mL}$ suspensions in water and subsequent deposition of 5 μL onto 200 mesh formvar/carbon-coated copper TEM grids which were then allowed to air dry. In addition to observing general morphology of the NPs, the mean particle size and standard deviation for each sample was calculated from measuring over 100 NPs in random fields of view using ImageJ software. The procedure was previously described by Murdock et al. (2008).

Dynamic Light Scattering (DLS) and Laser Doppler Velocimetry (LDV). Dynamic light scattering (DLS) and laser Doppler velocimetry (LDV), for characterization of size and zeta potential of the NPs in solution, were performed on a Malvern Instruments Zetasizer Nano-ZS instrument. DLS analyzes the velocity distribution of particle movement by measuring dynamic fluctuations of light scattering intensity caused by the Brownian motion of the particle. This technique yields a hydrodynamic radius, or diameter, to be calculated via the Stokes-Einstein equation from the aforementioned measurements. The measurement technique used by the Zetasizer Nano ZS to measure the zeta potential, or surface charge, of particles in a solution is known as Laser Doppler Velocimetry (LDV). This technique uses a laser as well, which is being passed through the sample to measure the velocity of the particles in an applied electric field to determine the electrophoretic mobility of the particle. The device uses a 4mW He-Ne 633 nm

laser to analyze the samples, as well as an electric field generator (for LDV measurements)⁷⁰. The Malvern Zetasizer Nano-ZS uses the Dispersion Technology Software (V4.20) for data collection and analysis. The mean particle diameter is calculated by the software from the particle distributions measured and the polydispersity index (PdI) given is a measure of the size ranges present in the solution (Malvern, 2005). The PdI scale ranges from 0 to 1, with 0 being monodisperse and 1 being polydisperse. The software calculates the PdI value from the G1 correlation function and from parameters defined in the ISO standard document 13321:1996 E. For all zeta potential measurements made, the Smoluchowski approximation was used since the particles were dispersed in polar solvents.

Samples were examined after dilution of NP stock solutions to 100 µg/mL suspensions in DI water, vortexed to provide a homogeneous solution, and then 1 mL was transferred to a Malvern Clear Zeta Potential cell for DLS and LDV measurements.

UV-Visible Absorption Spectroscopy (UV-Vis). The absorption spectra of the NMs were collected on the Cary UV-Vis 300 Spectrophotometer with WinUV software (Varian, Inc.). UV-Vis spectroscopy uses one or multiple light sources that can emit from the ultraviolet, through the visible, and sometimes into the near-infrared spectrums. The light is passed through a sample and the transmitted light is recorded by a detector. Any absorption of light by the sample is measured allowing identification of any specific wavelengths of absorbance which may be unique to that sample.

Samples were either measured at full stock concentration, half stock concentration, or a tenth of stock concentration depending on original particle stock concentration, and diluted using either DI H₂O or hybridization buffer (NaCl). This allowed the solution concentration to fall within the instrument's calibrated absorption measurement range. For spectrum scans, solutions were placed in quartz cuvettes for measurements, the chamber temperature was set at 25 °C, and the instrument was set to scan wavelengths from 200 nm to 800 nm.

Molar particle concentrations were calculated using the Beer-Lambert Law, $A = \epsilon lc$, where A is absorption in optical density units, ϵ is the extinction coefficient (at the surface plasmon wavelength) in L / (moles particles * cm), l is the light pathway length in cm (1 cm for all measurements performed), and c is the concentration in (moles particles) / L. For Au and Ag NPs, extinction coefficient values were obtained from literature sources^{45,71}.

Results

Transmission Electron Microscopy and Visual Solution Images. To observe the effects of the various synthesis techniques attempted on particle size and morphology, TEM was employed to visualize the materials and record a size distribution and general morphology for each batch. Results show the observation of solution color change as the 13 nm Au NPs are synthesized (Figure 3A), accompanied by selected TEM pictures to verify size and size distribution in Figures 3B and 3C. Primary particle mean size of three selected batches of the 13 nm Au NPs, as assessed by TEM, ranged from 12.6 nm to 13.7 nm (Table 1). All exhibited a SD less than 1 nm and spherical morphology (Table 1).

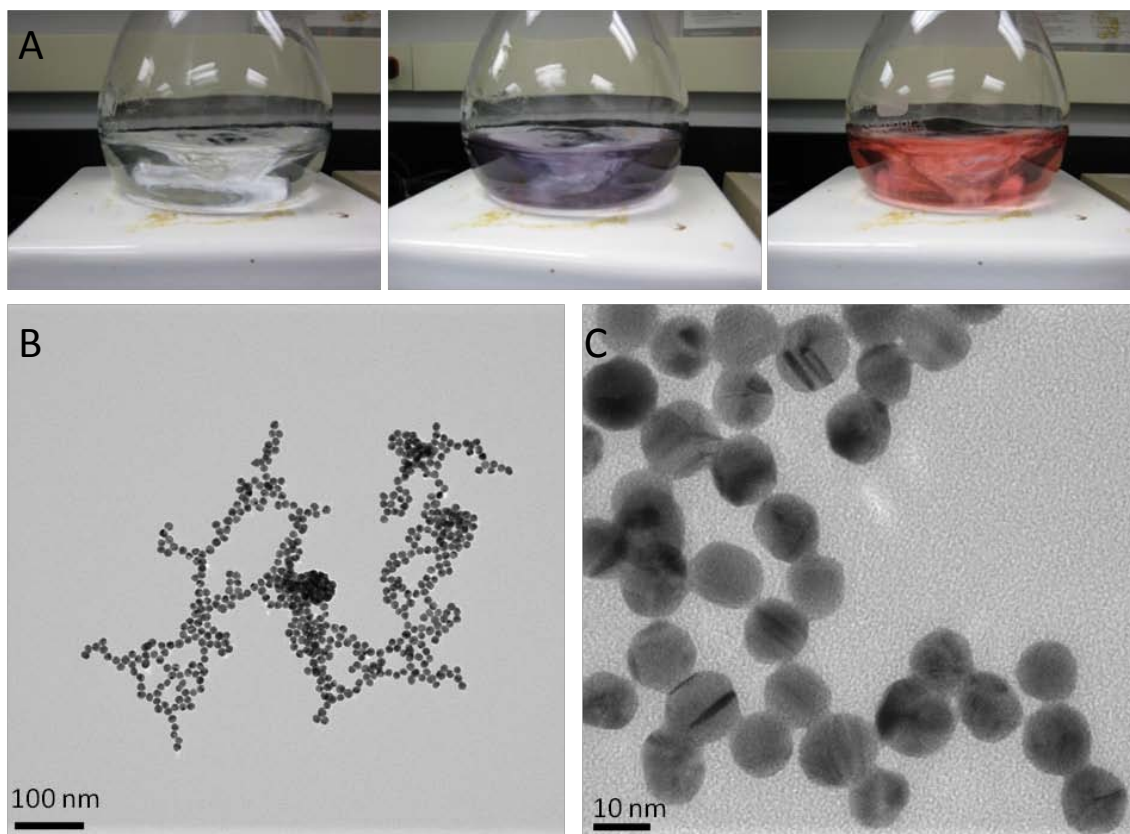


Figure 3. 13 nm Au Colloid Synthesis. (A) Digital images of solution during synthesis. (B) and (C) TEM images of 13 nm Au NPs post-synthesis.

In Figure 4A, visual images of the various batches synthesized to produce 4 nm Au NPs are shown, along with TEM images of selected batches. Batch 1 immediately turned a purplish color, indicating that the particles were roughly 50 nm in size or larger, so no further characterization was performed (data not shown). Batch 2 was successful in producing particles in the 4 nm size range with a mean primary particle size of 4.03 ± 1.22 nm and the particles were spherical in nature (Table 1, Figure 4B). For Batch 3, the particles produced were generally spherical and were found to have a mean primary particle size of 3.88 ± 1.14 nm (Table 1, Figure 4C). DLS results for batch 4 indicated that the majority of the particles were larger than 10 nm in size; hence further characterization was not performed or reported. Batch 5 was found to have a mean primary particle size of 3.55 ± 1.41 nm and spherical morphology (Table 1, Figure 4D).

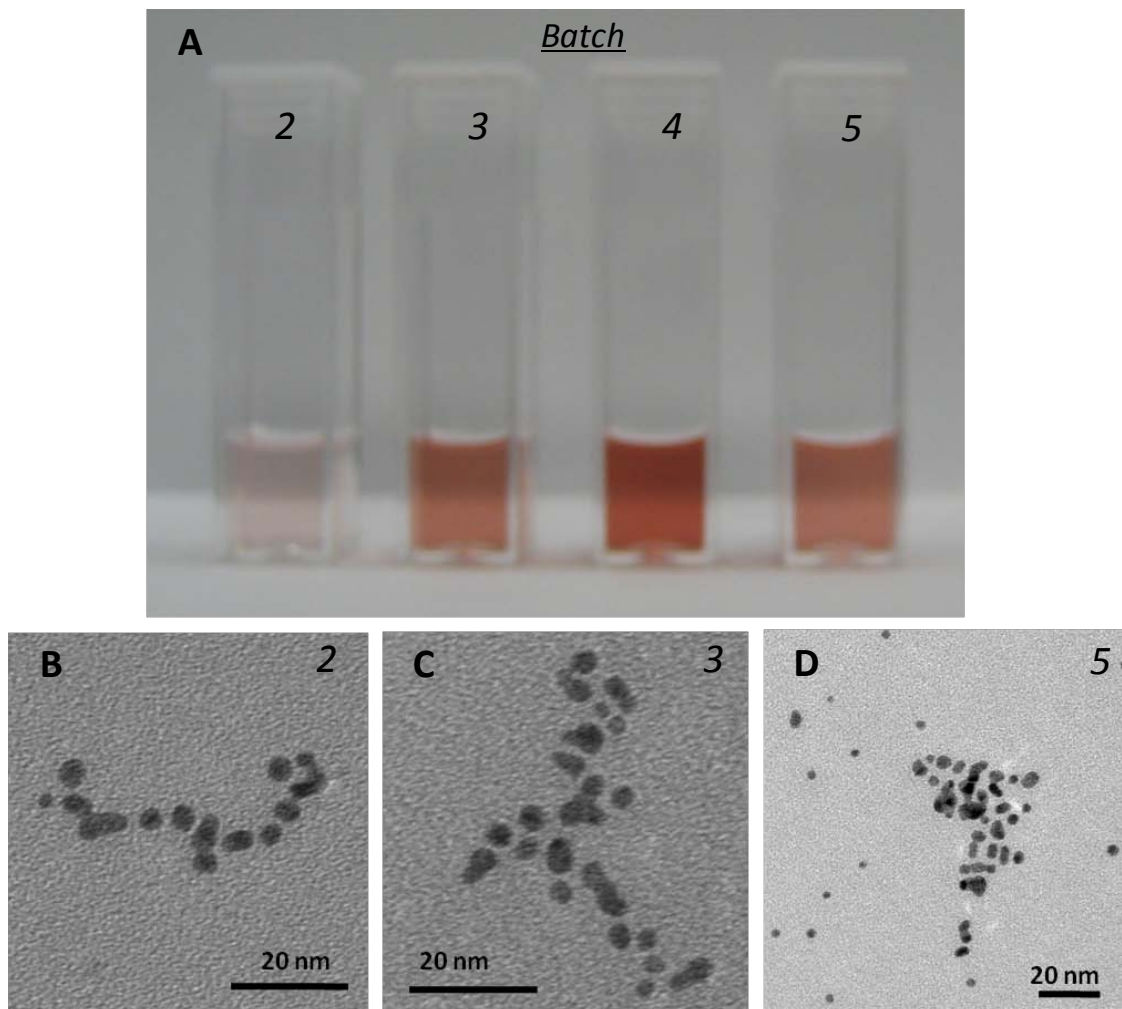


Figure 4. 4 nm Au Colloid Synthesis. (A) Digital images of batches 2, 3, 4, and 5. TEM images of batch 2 (B), batch 3 (C), and batch 5 (D).

For the 8 nm Ag NP synthesis, multiple batches and techniques were attempted to standardize the synthesis procedure, which are represented in Figure 5 with visuals of the various solutions as well as TEM images from selected batches. The color change of batch 1, shown in Figure 5A, indicated that larger particles were created and therefore no further characterization was performed. It was found during the synthesis of batch 1 that the solution is extremely sensitive to light during the reduction phase and for at least 10 min post reduction. For this reason, the following reactions were all performed in dark conditions with foil covering any storage containers. Batch 2 exhibited the proper solution color for Ag NPs around 10 nm in size, and TEM results confirmed this with a mean size of 7.37 ± 3.94 nm and spherical morphology (Table 1, Figure 5B). For Batch 3, PEG was added to the solution prior to reduction of the Ag ions and networks of smaller particles were formed. The smaller particles composing the network had a size distribution of 21.7 ± 5.37 nm with the overall networks being microns in size (Table 1, Figure 5C). Batches 4 and 5 produced fairly similar size distributions, with batch 4 at 10.4 ± 5.37 nm (Table 1, Figure 5D) and batch 5 13.5 ± 5.16 at nm (Table 1, not pictured) even using different synthesis techniques, with PEG being added to batch 5 as a secondary stabilizer

within 1 min after reduction of the Ag ions. Batch 6 was the same formulation and technique used for batch 4 and produce only slightly different results with a size distribution of 8.53 ± 3.92 nm (Table 1, Figure 5E).

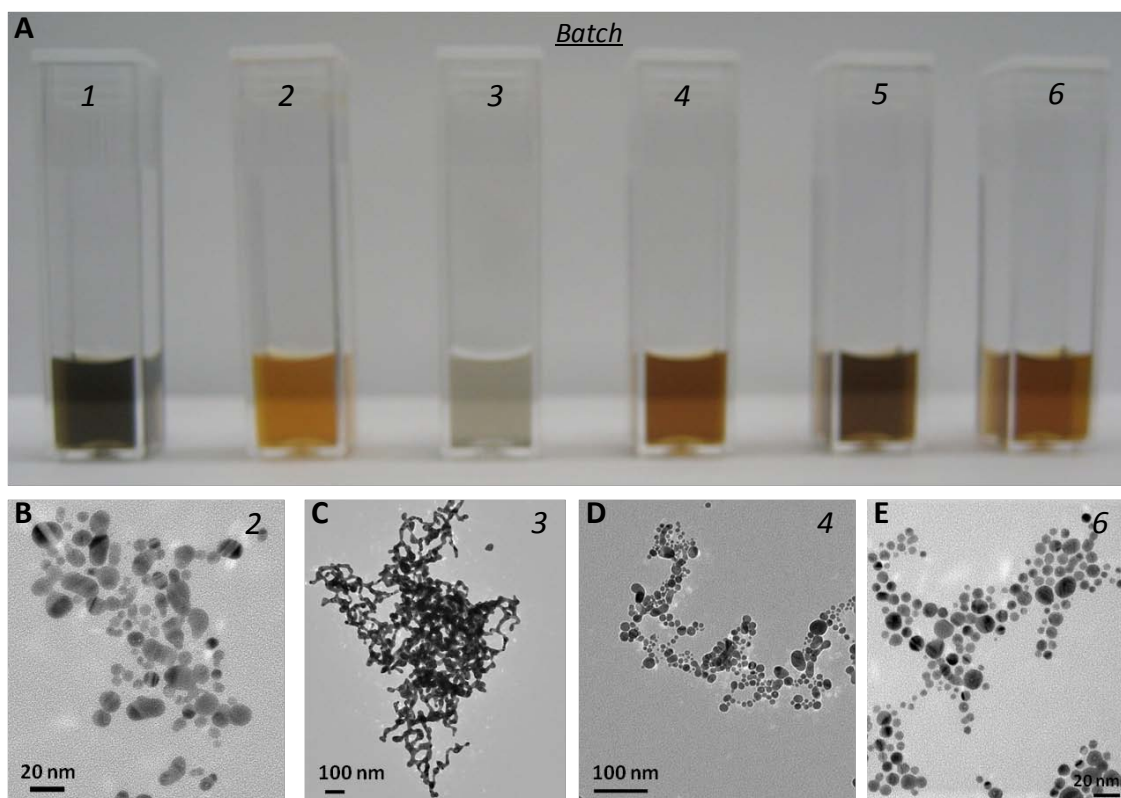


Figure 5. 8 nm Ag Colloid Synthesis. (A) Digital images of batches 1-6. TEM images of batch 2 (B), batch 3 (C), batch 4 (D), and batch 6 (E).

Dynamic Light Scattering. DLS results for select batches of each particle type made are shown in Table 1. For the 13 nm Au NPs, all three batches were very well dispersed with no agglomeration found which corresponded to the average hydrodynamic diameters of 15.7 nm, 15.3 nm, and 12.9 nm for batches 1, 2, and 3, respectively. The three batches synthesized of the 4 nm Au NPs were in very close agreement with each other with average diameters of 4.99 nm (batch 2), 3.58 nm (batch 3), and 5.25 nm (batch 5), indicating no aggregation of the particles in solution. Due to the different synthesis techniques attempted for the 8 nm Ag NPs, there was more variability experienced with the DLS measurements. For batch 2, an average hydrodynamic diameter of 16.1 nm was found. Batches 3 and 5 both had PEG added to the synthesis process; however, the PEG was added before reduction in batch 3 and after reduction for batch 5, which produced drastically different results with a mean size of 256 nm for batch 3 and 12.5 nm for batch 5. These results correlate to the TEM results presented previously. Batch 4 had an average size of 13.3 nm in solution, indicating no agglomeration with this sample as well. Batch 6 was found to have a similar average particle size in solution of 11.7 nm.

Zeta potential values were only measured for the last batch produced in the synthesis process, since this was the final synthesis technique determined and those particles would be

used for the following functionalization procedures. The 13 nm Au, 4 nm Au, and 8 nm Ag NPs were all found to have highly negative zeta potentials at -45.9 mV, -37.4 mV, and -47.2 mV, respectively, which indicated very stable suspensions of particles for all samples (Table 1). This is expected since all had similar final surface chemistry from similar reduction and stabilizing chemicals.

Table 1. Dynamic Light Scattering (DLS) and Laser Doppler Velocimetry (LDV) Results for Various Batches of Synthesized Colloids.

Particle	TEM	DLS	LDV
	Size Distribution <i>Mean ± SD</i> (nm)	Z-Average Diameter (nm)	Zeta Potential ζ (mV)
13 nm Au NPs			
Batch 1	13.7 ± 0.71	15.7	***
Batch 2	13.5 ± 0.85	15.3	***
Batch 3	12.6 ± 0.96	12.9	-45.9
4 nm Au NPs			
Batch 2	4.03 ± 1.22	4.99	***
Batch 3	3.88 ± 1.14	3.58	***
Batch 5	3.55 ± 1.41	5.25	-37.4
8nm Ag NPs			
Batch 2	7.37 ± 3.94	16.1	***
Batch 3	21.7 ± 5.37	256	***
Batch 4	13.5 ± 5.16	13.3	***
Batch 5	10.4 ± 4.21	12.5	***
Batch 6	8.53 ± 3.92	11.7	-47.2

UV-Vis Spectroscopy. The UV-Vis spectra obtained for the 13 nm Au NPs is shown in Figure 6. The LSPR is the absorbance of a specific wavelength of light by a NP which induces electromagnetic oscillations on the surface. LSPRs for noble metal NPs, such as Au and Ag, exhibit much stronger absorption bands than in their bulk counterparts. The absorption maxima for the 13 nm Au NPs occurred at a wavelength of 520 nm, which correlates well to literature values⁷⁰. Using an extinction coefficient of $1.39 \times 10^8 \text{ M}^{-1} \text{ cm}^{-1}$ (70), the molar particle concentration was determined to be ~10 nM.

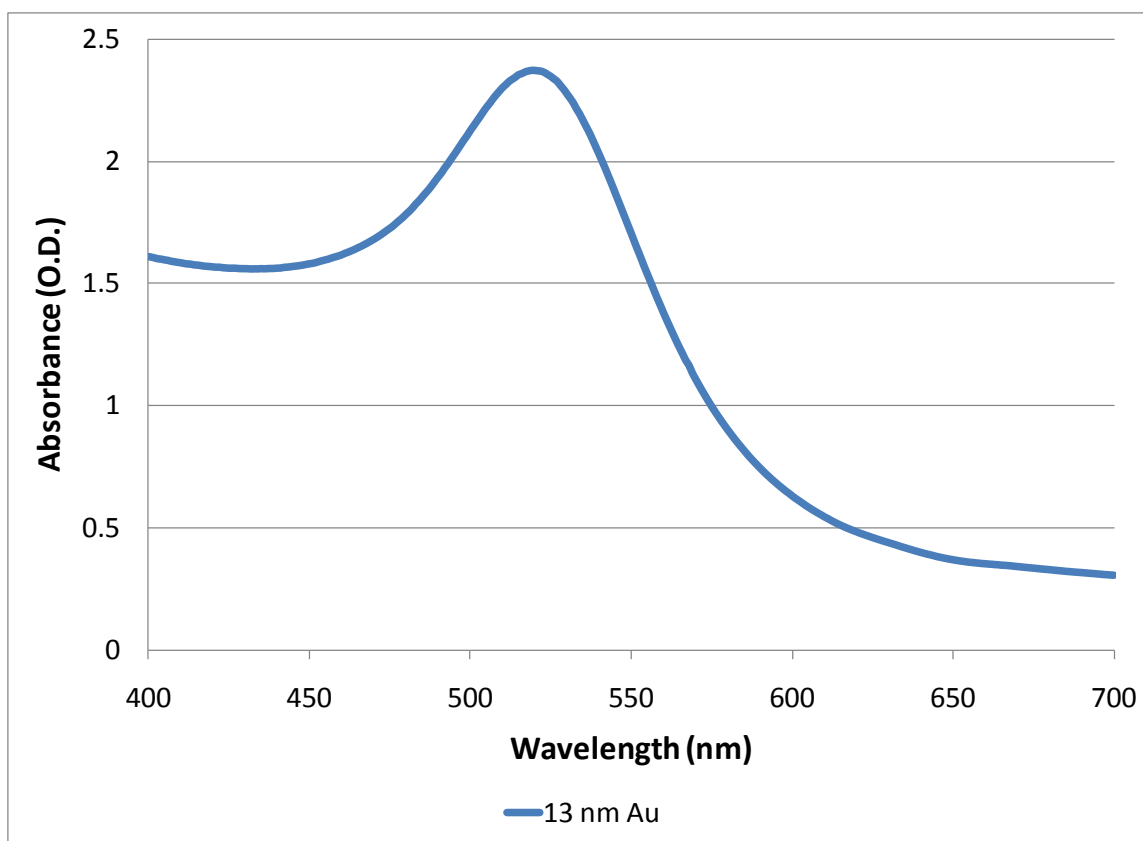


Figure 6. UV-Vis Absorption Spectra of 13 nm Au Colloid Batch 3.

The absorption maxima for the 4 nm Au NPs batches, which are shown in Figure 7, were 509 nm (batch 2), 505 nm (batch 3), 508 nm (batch 4), and 506 nm (batch 5). Batches 3 and 5 compare well to theoretical values and also demonstrate the blue-shift of the LSPR peak as particle size decreases when compared to the 13 nm Au NP spectra. The A_{SPR}/A_{450} ratio for batch 5 is also in good agreement with literature values at 1.18 compared to a value of 1.19 which was theoretically determined^{71,72}. Using an extinction coefficient of $3.62\text{E}6 \text{ M}^{-1}\text{cm}^{-1}$ (70) and the Beer-Lambert Law, the molar particle concentration for batch 5 was determined to be ~167 nM.

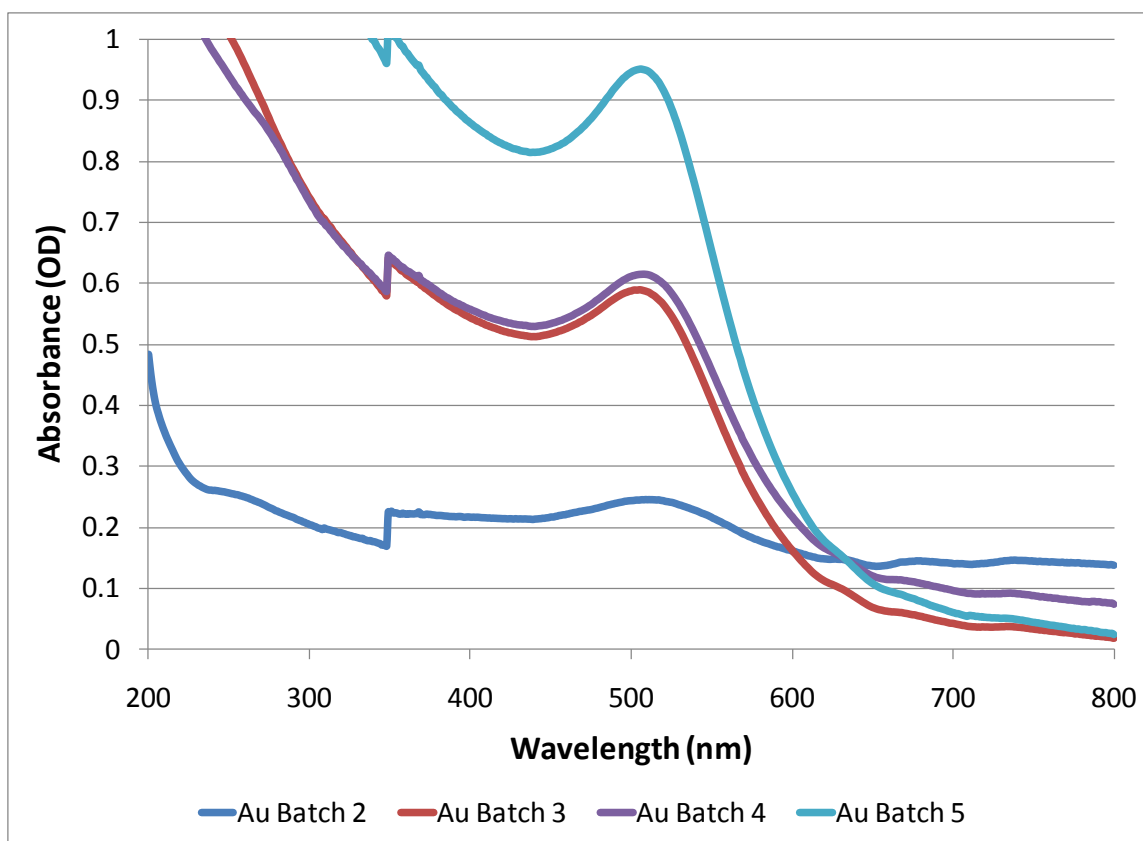


Figure 7. UV-Vis Absorption Spectra of 4 nm Au Colloid Batches 2, 3, 4, and 5.

The absorption spectra for the various Ag NP batches are shown in Figure 8 with the absorption maxima occurring at 394 nm for batch 1, 390 nm for batches 2 and 4, 388 nm for batch 5, and 389 nm for batch 6. Batches 2, 4, and 6 coincide with literature values for similarly sized Ag NPs. There are few publications concerning extinction coefficients for various sizes of Ag; therefore, the extinction coefficient used was $4.83\text{E}9 \text{ M}^{-1}\text{cm}^{-1}$, which was extrapolated by Sebba et al. (2008(2)) using Mie Theory for a similarly sized Ag NP, and the molar particle concentration for batch 6 was $\sim 16.5 \text{ nM}$.

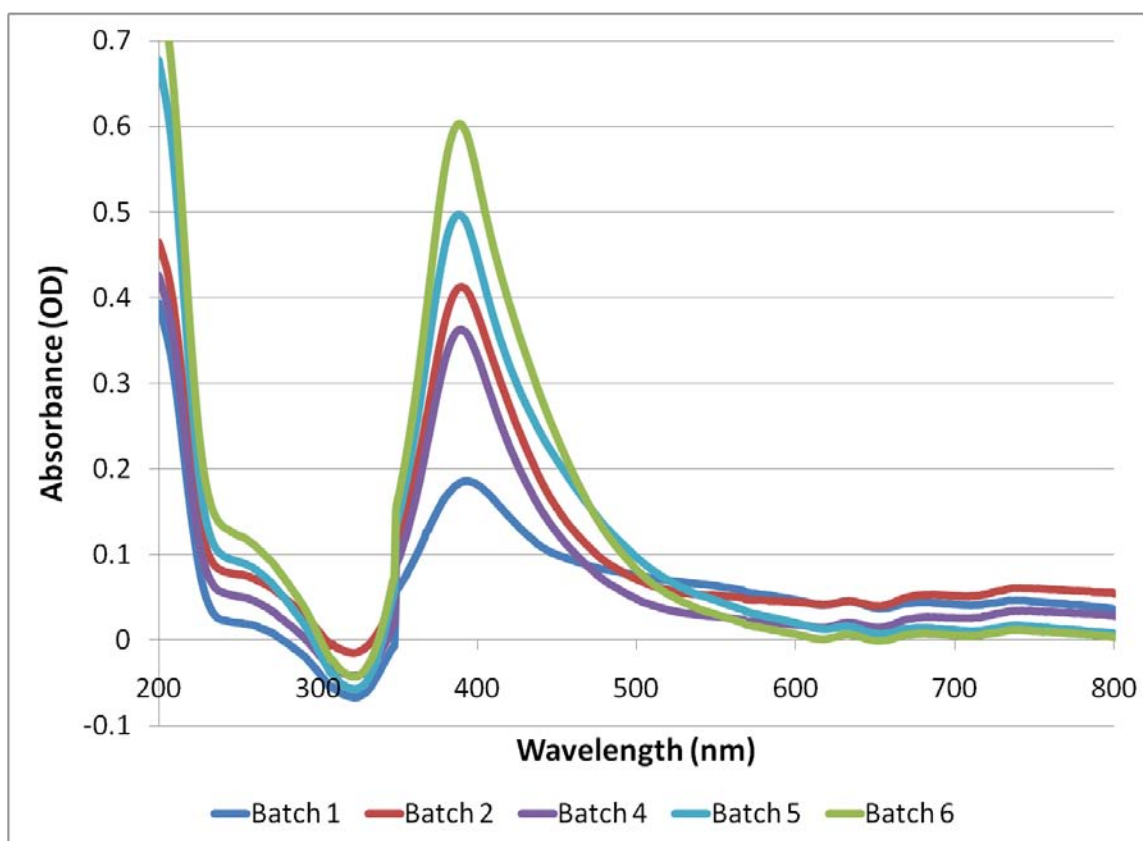


Figure 8. UV-Vis Absorption Spectra of Ag Colloid Batches 1, 2, 4, 5, and 6.

Discussion

One of the objectives of this research was to produce Au and Ag colloids in the 5-8 nm size range for the purpose of enhancing uptake into the nucleus since nuclear membrane pores have shown to be approximately 9 nm in size⁷³. However, producing uniform particles of any material in the sub-10 nm regime presents new challenges. For most of the initial work done on this project, 13 nm Au NPs were synthesized by the well known Turkevich method with very high uniformity and reproducibility (Figure 3, Table 1).

Several techniques are available in the literature for the synthesis of 4-5 nm Au NPs; however, they required the use of organic solvents with complicated ligand exchange processes for biofunctionalization. It was desired to have a biocompatible particle which would also be easy to functionalize, such as containing a citrate layer on the surface. Batch 1 was unsuccessful at producing nanometer sized particles due to the reaction being carried out at room temperature. For most NP synthesis methods using sodium citrate and sodium borohydride reductions, the temperature at which the reaction occurs can have a large impact on the size produced. For example, to produce smaller NPs, sodium borohydride and low solution temperatures must both be used⁶⁵. If using sodium citrate, high temperatures must be used to achieve smaller particles⁶³. After this finding, all subsequent batches were synthesized at a solution temperature of 4°C. Batch 2, successfully synthesized Au NPs in the 4 nm size range; however, the concentration of the solution was too low to be useful for functionalization studies (Figure 4B). The initial chloroauric acid concentration was doubled for batch 3 as compared to batch 2, and was

successful in producing 4 nm Au NPs at a higher particle concentration without impacting overall particle quality (Figure 4C). In an effort to further improve end particle concentration, the initial chloroauric acid concentration was again doubled for batch 4; however, this procedure produced particles above 10 nm in size and therefore was not a viable option. Batch 5 followed the same procedure as batch 3 to verify the synthesis procedure and results, which confirmed the procedure was the best option (Figure 4D). In summary, it was found that extremely uniform and reproducible 4 nm Au NPs can be formed by using a sodium borohydride reduction of chloroauric acid in water at 4°C, followed by addition of sodium citrate which exchanges surface ions and helps to stabilize the solution. For this reason, the synthesis method used for batch 5 was adopted as the standard procedure for 4 nm Au NPs (Figure 4D). As far as long term stability of the particles, particle solutions have shown no change even 4 months post synthesis.

A similar method was attempted to synthesize Ag NPs. On average, 8 nm Ag NPs were formed with fairly good consistency, yet the uniformity of the NPs was not as superior as the Au samples (Figure 5, Table 1). During the synthesis of batch 1, the Ag synthesis process was found to be extremely sensitive to small temperature variations and any exposure to light during the process, which appeared to be the main causes for the inconsistencies of batch 1. To correct for these issues, batch 2 was synthesized in solutions kept at 4°C and also kept in minimal light conditions by covering the reaction beaker in foil and turning off room lighting. These changes proved to be successful for synthesizing particles in the sub-10nm range; however the uniformity of the particles produced was not as successful. In an attempt to lessen the size deviation, polyethylene glycol (PEG) was added to batch 3 in the silver nitrate solution prior to reduction and yielded an interesting outcome in which micron sized networks of fused 20 nm particles were produced. Batch 4 was a reiteration of the method used for batch 2 at double the initial silver nitrate concentration, and did produce NPs, but they were outside the sub-10 nm regime needed. It was later determined that the issue with batch 4 was the use of not freshly prepared sodium borohydride. For batch 5, the addition of PEG to the solution was attempted again; however, this time it was added immediately post reduction. It was found that this helped to reduce the average particle size into the sub-10 nm size range, but there was still a large discrepancy in the sizes present in the sample. Batch 6 was identical to the method used for batch 4, except for the sodium borohydride used was prepared just prior to synthesis of the Ag NPs and the temperature of the solution was maintained vigilantly at 4°C. As a result of these modifications, batch 6 produced an average size of 8.5 nm with reduced size variability within the sample and was chosen to be the standard method used. The particle solutions are quite stable after about 24 h post synthesis and can even be exposed to light for extended periods of time without any observed particle morphology or size changes. However, the Ag NPs were observed to slightly settle after about 3 months, but it appears to only be the slightly larger particles settling, since the solution displays a color gradient and no precipitates were formed. The NP solutions redispersed readily once vortexed. In summary, an easy method of synthesis was found to produce Au and Ag NPs near the 5-8 nm range intended. This method left a citrate capping layer on the surface to enhance solution stability and facilitate biofunctionalization of the NPs.

FUNCTIONALIZATION OF NANOMATERIALS

Materials and Methods

Oligonucleotides. Two complementary sets of oligonucleotides were obtained from Integrated DNA Technologies, Inc. Sequence A1 (5'- HS-AAAAAAAAAACGCATTCAGCATTCT -3') and sequence C1 (5'- HS-AAAAAAAAAAGAATCCTGAATGCG -3') are complementary and both contain a poly-A spacer. Sequence A1-pA (5'- HS-CGCATTCAGCATTCT -3') and sequence C1-pA (5'- HS-AGAATCCTGAATGCG - 3') are complementary and are lacking the poly-A spacer. All sequences contain a thiol modification (HS-) at the 5' end of the sequence. This thiol modification allows the oligonucleotide to bond to the surface of the Au or Ag NPs by displacing the H^+ and forming a bond between the surface atoms and the S molecule, which has nearly the binding energy of a disulfide bond^{18,19}. In all NPs functionalized, the thiolated oligonucleotides are attached to the surface of the NP through a salt concentrating procedure which forces the oligonucleotides and NPs into close proximity, allowing the attachment to occur with better coverage of the NPs. The functionalization methods used for the Au and Ag NPs were adapted from similar literature procedures^{41,43-45,64,69} and an overview of the functionalization procedure is presented in Figure 9. The oligonucleotides were received in lyophilized form and were resuspended in 10 mM Tris Acetate (pH 7.4), or Tris (Hydroxymethyl) Aminomethane (Sigma), to a stock concentration of 1 mM. Finally, 20 μ L of each DNA sequence was aliquoted into microcentrifuge tubes and stored at -20°C.

Functionalization of 13 nm Gold Colloid. To standardize the functionalization procedure for the following colloidal materials, the 13 nm Au colloids were chosen to begin with since they are easily functionalized and do not require any special centrifugation. First, the 13 nm Au NPs, 3 mL of ~13 nM NPs were placed into scintillation vials separately for each DNA sequence. Next, 20 μ L of each 1 mM DNA sequence was added to the different scintillation vials while stirring briefly. The mixture was then let sit in the dark for 20 min without stirring. Following this, 366 μ L of 100 mM potassium phosphate buffer (PB) (Sigma) was added to each mixture, and 55 μ L of 2 M NaCl (Sigma) solution was added to each Au-DNA mixture every 20 min (5 times) until a total of 275 μ L had been dispensed. The Au-DNA mixture was left at room temperature overnight in the dark. The Au-DNA mixtures were then aliquoted, 500 μ L each, into multiple microcentrifuge tubes (6 tubes per DNA sequence) and centrifuged at 16,000 x g for 14 min. The supernatant was removed and each pellet was resuspended in 100 μ L of 100 mM NaCl, 25 mM Tris Acetate (pH 8.2) solution and centrifuged at 16,000 x g for 12 min. Again, the supernatant was removed and the pelleted material was resuspended in 100 μ L of 100 mM NaCl, 25 mM Tris Acetate (pH 8.2) solution. The samples were centrifuged a final time at 16,000 x g for 12 min. The supernatant was removed, and the pellets were this time resuspended in hybridization buffers of different NaCl concentrations dependent upon the melting temperature, or dehybridization temperature, desired. For the 13 nm Au-DNA NPs, this was either 100 μ L of 50 mM NaCl, 25 mM Tris Acetate (pH 8.2) or 100 μ L of 100 mM NaCl, 25 mM Tris Acetate (pH 8.2) solutions. After resuspension in the proper hybridization buffer, the samples with the same DNA functionalization were combined into one microcentrifuge tube for storage. A sample of each Au-DNA mixture was measured by UV-Vis spectroscopy to

determine the concentration of each solution. Using this information, equimolar amounts of each complementary Au-DNA samples were combined in a new microcentrifuge tube and stored at 4°C overnight for hybridization. During the hybridization process, a NP with one complementary oligonucleotide sequence on the surface is linked to another NP with the other oligonucleotide sequence, forming a short double stranded DNA sequence bond between the NPs. Since the oligonucleotides are covering the surface of the spherical NP, they can create bonds with other NPs in any dimension allowing for the possibility of larger 3-dimensional structures to be formed. The following day, the samples were vortexed to resuspend any settled aggregates of NPs prior to use.

Functionalization of 4 nm Gold Colloid. To functionalize the 4 nm Au NPs, 3 mL of ~130 nM NPs were placed into scintillation vials separately for each DNA sequence. Next, 40 µL of each 1 mM DNA sequence was added to the different scintillation vials while stirring briefly. The mixture was let sit in the dark for 20 min without stirring. Following this, 366 µL of 100 mM PB was added to each mixture, and then 55 µL of 2 M NaCl solution was added to each Au-DNA mixture every 20 min (5 times) until a total of 275 µL had been dispensed. The Au-DNA mixture was left to rest at room temperature overnight in the dark. It was determined that standard centrifugation, or less than 20,000 x g, was unable to pellet any significant amount of the sample; therefore ultracentrifugation was required for this size NP. The ultracentrifugation speed used in the procedure was determined by experimental process to reach an optimal region where pelleting of the smaller NPs occurs without permanent NP-to-NP adhesion, allowing for resuspension of the NPs. The Au-DNA mixtures were aliquoted, 1500 µL each, into multiple ultracentrifuge tubes (2 tubes per DNA sequence) and ultracentrifuged at 261,600 x g for 20 min. The supernatant was removed and each pellet was resuspended in 200 µL of 100 mM NaCl, 25 mM Tris Acetate (pH 8.2) solution and centrifuged at 261,600 x g for 20 min. The supernatant was removed and the pelleted material was again resuspended in 200 µL of 100 mM NaCl, 25 mM Tris Acetate (pH 8.2) solution. The samples were centrifuged a final time at 261,600 x g for 20 min. The supernatant was removed, and the pellets were resuspended in hybridization buffers of different NaCl concentrations dependent upon the dehybridization temperature desired. For the 4 nm Au-DNA NPs, this was either 200 µL of 300 mM NaCl, 25 mM Tris Acetate (pH 8.2) or 200 µL of 500 mM NaCl, 25 mM Tris Acetate (pH 8.2) solutions. After resuspension in the proper hybridization buffer, the samples with the same DNA functionalization were combined into one microcentrifuge tube for storage. A sample of each Au-DNA mixture was measured by UV-Vis spectroscopy to determine the concentration of each solution. Using this information, equimolar amounts of each complementary Au-DNA samples were combined in a new microcentrifuge tube and stored at 4°C overnight for hybridization. The following day, the samples were vortexed to resuspend any settled aggregates of NPs prior to use.

Functionalization of 8 nm Silver Colloid. For functionalization of the 8 nm Ag NPs, 3 mL of ~15 mM NPs were placed into scintillation vials separately for each DNA sequence. Next, 40 µL of each 1 mM DNA sequence was added to the different scintillation vials while stirring briefly. The mixture was left in the dark for 20 min without stirring. Following this, 366 µL of 100 mM PB was added to each mixture, and then 55 µL of 2 M NaCl solution was added to each Ag-DNA mixture every 20 min (5 times) until a total of 275 µL had been dispensed. The Ag-DNA mixture was left to rest at room temperature overnight in the dark. For this NP, it was

determined that standard centrifugation was necessary to pellet Ag NPs in the sample which were larger than ~10 nm in size. The supernatant containing smaller than ~10 nm Ag NPs was removed and washed using ultracentrifugation. This was accomplished by first aliquoting the Ag-DNA mixtures into multiple microcentrifuge tubes (500 μ L each, 6 tubes per DNA sequence), and centrifuged at 12,000 x g for 14 min. The supernatant was removed, transferred, and combined into 2 ultracentrifuge tubes per DNA sequence. From this point forward, the samples were treated as 2 different sets. The ultracentrifugation speed chosen was determined by experimental process to reach an optimal region where pelleting of the smaller NPs occurs without permanent NP-to-NP adhesion, allowing for resuspension of the NPs. The procedures for the standard centrifuged set and ultracentrifuged set are as follows.

For the standard centrifuged samples, each pellet was then resuspended in 100 μ L of 100 mM NaCl, 25 mM Tris Acetate (pH 8.2) solution and centrifuged at 12,000 x g for 12 min. The supernatant was removed as much as possible and then the pelleted material was again resuspended in 100 μ L of 100 mM NaCl, 25 mM Tris Acetate (pH 8.2) solution. The samples were then centrifuged a final time at 12,000xg for 12 min.

For the ultracentrifuged samples, the supernatants which were transferred into multiple ultracentrifuge tubes (2 tubes per DNA sequence) were ultracentrifuged at 174,400 x g for 20 min. The supernatant was removed and each pellet was then resuspended in 200 μ L of 100 mM NaCl, 25 mM Tris Acetate (pH 8.2) solution and centrifuged at 174,400 x g for 20 min. Again, the supernatant was removed and the pelleted material was resuspended in 200 μ L of 100 mM NaCl, 25 mM Tris Acetate (pH 8.2) solution. The samples were centrifuged a final time at 174,400 x g for 20 min.

The final steps of the procedure for each set of samples were the same. The supernatant was removed from all samples, and the pellets were this time resuspended in hybridization buffers of different NaCl concentrations dependent upon the dehybridization temperature desired. For the 8 nm Ag-DNA NPs, this was either 200 μ L of 300 mM NaCl, 25 mM Tris Acetate (pH 8.2) or 200 μ L of 500 mM NaCl, 25 mM Tris Acetate (pH 8.2) solutions. After resuspension in the proper hybridization buffer, the samples with the same DNA functionalization were combined into one microcentrifuge tube for storage. A sample of each Au-DNA mixture was measured by UV-Vis spectroscopy to determine the concentration of each solution. Using this information, equimolar amounts of each complementary Au-DNA samples, respective to the centrifuging process used as well, were combined in a new microcentrifuge tube and stored at 4°C overnight for hybridization. The samples were vortexed to resuspend any settled aggregates of NPs prior to use.

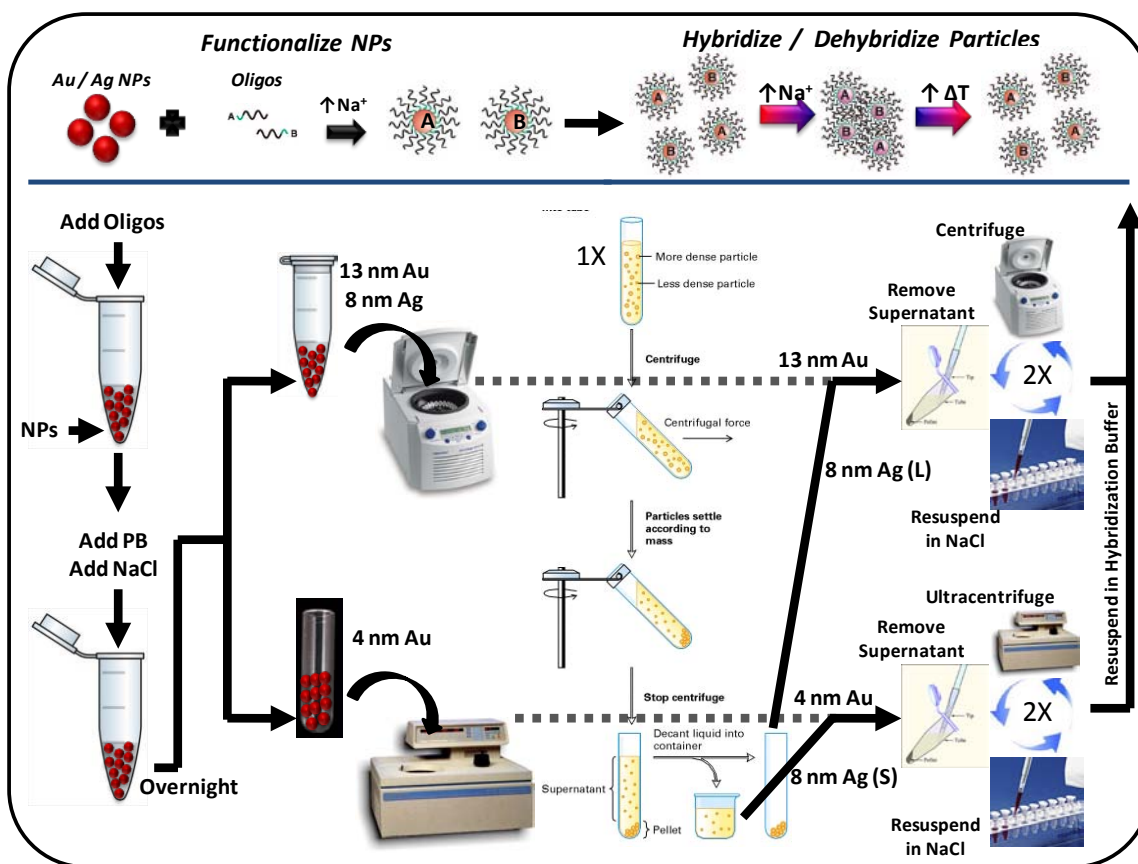


Figure 9. Diagram of Functionalization Procedure.

Characterization of Functionalized Gold and Silver Colloids

Transmission Electron Microscopy (TEM). To characterize functionalized and hybridized NPs, TEM characterization was performed to verify that the functionalization process had not altered the NPs in any way and to observe successful hybridization. Functionalized and hybridized NPs were diluted 1:10 using the proper hybridization buffer, and 5 μ L was deposited onto formvar/carbon-coated copper TEM grids as previously described on page 9.

Dynamic Light Scattering (DLS). DLS was used to measure size changes of the NPs after functionalization or hybridization. Samples were diluted in hybridization buffer as previously described in on page 9.

UV-Vis Spectroscopy (UV-Vis). The absorption spectra of the functionalized NMs and DNA dehybridization curves were collected using UV-Vis. Samples were diluted to half concentration or a tenth of original concentration using hybridization buffer as previously described in on page 10. Prior to hybridization of the samples, equimolar NP concentrations were using ratios of the absorbance values (optical density; O.D.). For thermal scans, the solutions were also placed in a quartz cuvette, but the instrument was set to scan a single wavelength of 280 nm and the temperature was increased at steps of 2 $^{\circ}$ C every 2 min recording any change in the absorption at this wavelength.

Hyperspectral Imaging. Hyperspectral Imaging (HSI) was performed on certain samples as a potential methodology for detecting NP state in a biological system in future studies. HSI collects a spectra similar to that of UV-Vis, except that the spectra obtained is for reflected light from the sample instead of the absorbed spectra as in UV-Vis and can provide just as unique information about the sample. Samples were prepared by spotting 10 μ L of the stock solution onto a glass microscope slide, applying a cover glass, and sealing the cover glass with clear nail polish around the edges. The slide was then let sit for 30 min to 1 h to allow the NPs to settle so they could be scanned properly on the CytoViva Hyperspectral Imaging System (HSI). Scan information was collected and processed through ENVI software.

Results

Transmission Electron Microscopy and Solution Images. Functionalization results of the 13 nm Au NPs are shown in Figure 10. Images of the 13 nm Au NPs functionalized with different oligonucleotide sequences and the hybridized NP solutions are represented in Figure 10A. Assessing the color of each solution alone at critical steps in the process yeilds valuable information about the success of the functionalization. All individually functionalized 13 nm Au NPs, A1, C1, A1-pA, and C1-pA, all demonstrated the crimson red appearance of the original 13 nm Au NPs, but at a higher concentration (Figure 10A). This indicated that the NPs were not significantly altered during the process and also that the NPs were still well dispersed, both of which would have been shown by a color shift in the solution. A representative TEM image is shown in Figure 10B of the 13 nm Au A1 NPs, which demonstrates the NPs were not significantly changed by the functionalization process. However, the hybridized samples (A1+C1, A1-pA+C1-pA, A1+C1-pA, and C1+A1-pA) indicated proper hybridization by exhibiting the blue color shift (Figure 10A). TEM was used to visualize the hybridized NPs, in this case the 13 nm Au A1+C1 NPs, which demonstrates the large networks of NPs that are formed when the DNA hybridizes (Figure 10C). Fairly uniform spacing of \sim 1-3 nm is obseved (Figure 10D). Figure 10D is a higher magnification image of the red highlighted area in Figure 10C.

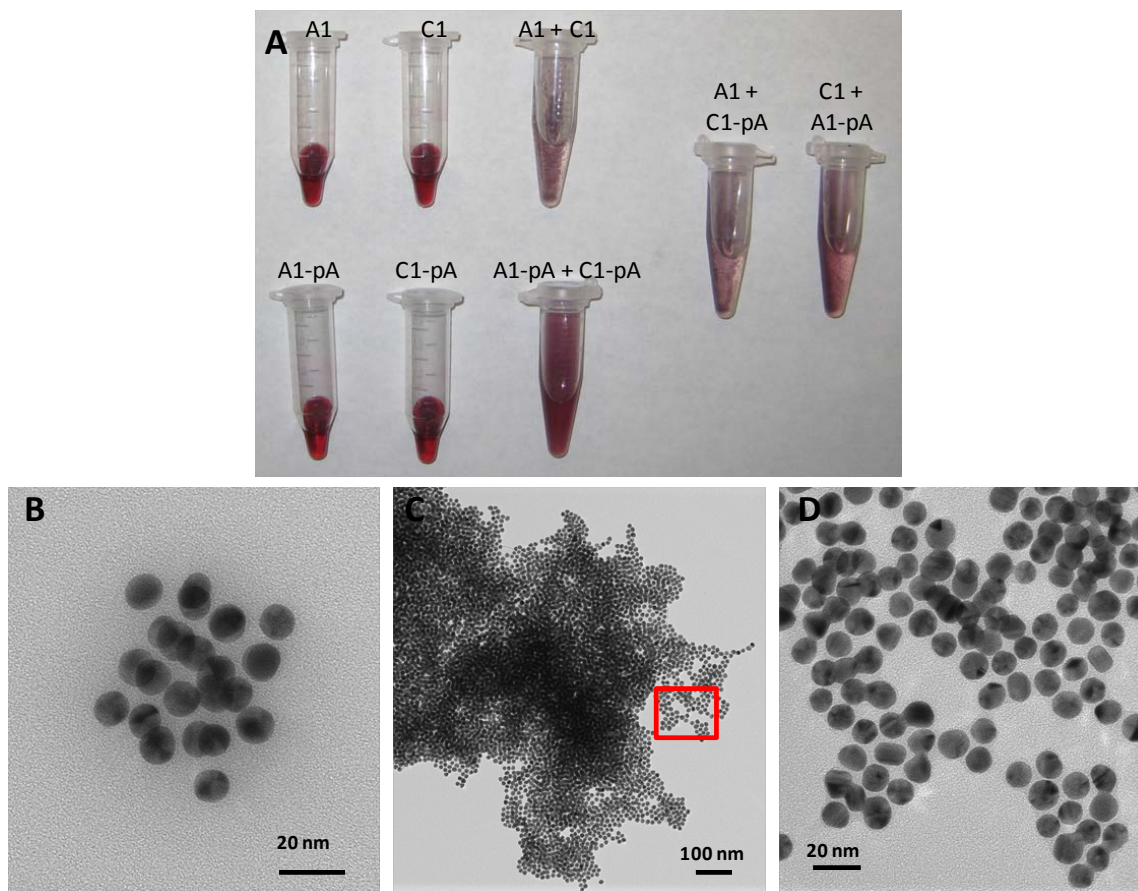


Figure 10. Functionalized and Hybridized 13 nm Au NPs. (A) Digital images of the functionalized and hybridized solutions. (B) TEM image of the functionalized 13 nm Au A1 NPs. (C) TEM image of the hybridized 13 nm Au A1+C1 NPs. (D) Higher magnification TEM image of the red highlighted area in (C).

TEM images of the functionalized and hybridized 4 nm Au NPs and 8 nm Ag NPs are shown in Figure 11. The hybridized, standard centrifuged 8 nm Ag A1+C1 NPs were found to form smaller networks of NPs, approximately 300 to 500 nm in size, as can be seen in Figure 11A. The 4 nm Au A1+C1 NPs formed networks 200 to 300 nm in size (Figure 11B), with the high salt concentration necessary to hybridize these NPs evident in the image. The 4 nm Au A1-pA+C1-pA NPs formed large, tightly packed networks microns in size (Figure 11C) with salt residue visible under TEM for this sample also. The difference in the oligonucleotide lengths, due to the presence of the poly-A sequence, can be observed when comparing the interparticle spacing of the 4 nm Au A1+C1 NPs to the 4 nm Au A1-pA+C1-pA NPs (Figures 11B and 11C).

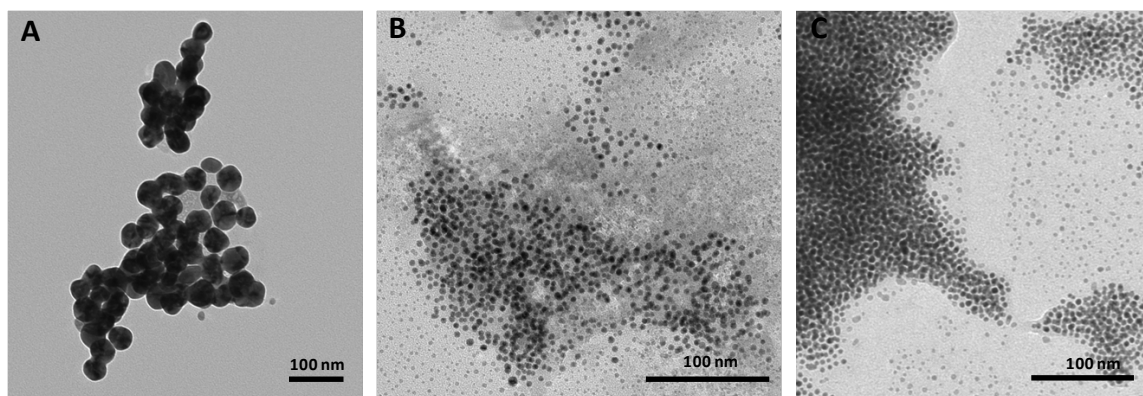


Figure 11. Hybridized Ag and Au NPs. (A) TEM image of the hybridized 8 nm Ag A1+C1 NPs. (B) TEM image of the hybridized 4 nm Au A1+C1 NPs. (C) TEM image of the hybridized 4 nm Au A1-pA+C1-pA NPs.

Dynamic Light Scattering. DLS was used to verify an increase in NP diameter once the oligonucleotides were attached to the NPs and to observe agglomeration trends. The measurements were only performed on the initial functionalization batches of the 13 nm Au NPs as verification of NP coverage and were not deemed necessary to perform later on the 4 nm Au NPs and the 8 nm Ag NPs. The results for these measurements are displayed in Table 2. The unfunctionalized 13 nm Au NPs had an average hydrodynamic diameter of 15.3 nm, which increased to 39.7 nm and 33.9 nm once functionalized with the A1 and C1 sequences, respectively. However, the A1-pA and C1-pA functionalized NPs only increased to 21.1 nm and 27.7 nm in diameter, which shows the difference in the overall NP diameter when the poly-A sequence is present or not. The two hybridized samples, A1+C1 and A1-pA+C1-pA, were measured as well to look at the aggregate sizes in solution. The asterisk next to the Z-Ave value for the A1+C1 sample denotes that even though an average agglomerate size of 599 nm was found, visually this sample had the higher aggregation of the two samples. The reading was skewed due to the aggregates settling rapidly out of solution before a complete measurement run could be made, thus shifting the observed average size by the DLS. The A1-pA+C1-pA hybridized sample had an average aggregate size of 2080 nm.

Table 2. Dynamic Light Scattering (DLS) Results for Unfunctionalized, Functionalized, and Hybridized 13 nm Au NPs.

<i>Sample Name</i>	<i>Z-Ave (d.nm)</i>	<i>Pdl</i>	<i>Pdl Width (d.nm)</i>
<i>Particle Only</i>			
13 nm Au	15.3	0.127	5.46
<i>Functionalized Particles</i>			
A1	39.7	0.211	18.2
C1	33.9	0.193	14.9
A1-pA	21.1	0.126	7.47
C1-pA	27.7	0.231	13.3
<i>Hybridized Particles</i>			
A1 + C1	599*	0.56	448
A1-pA + C1-pA	2080	0.45	1400

UV-Vis Spectroscopy. UV-Vis spectroscopy was used to observe the functionalization of the NPs, where a red-shift in the SPR is observed when molecules are attached to Au and Ag NPs. Figure 12 shows the normalized spectra of each functionalized NP as compared to the unfunctionalized NP. The unfunctionalized 13 nm Au NPs were previously found to have a SPR peak at 520 nm, but when the DNA is attached via thiol-linkage to the surface, the peak is shifted to 522 nm (A1), 523 nm (C1), 522 nm (A1-pA), and 522 nm (C1-pA) (Figure 12A). In Figure 12B, the unfunctionalized 4 nm Au NPs had an SPR peak at 506 nm, with the functionalized NPs' peak shifting to 519 nm (A1), 518 nm (C1), 517 nm (A1-pA), and 520 nm (C1-pA), which was the largest observed spectra shift of the three NPs. The 8 nm Ag NPs normally have a SPR peak at 389 nm; however, when functionalized the peaks shift to 395 nm (A1), 396 nm (C1), 394 nm (A1-pA), and 396 nm (C1-pA) (Figure 12C). In addition to looking for the spectral peak shifts, it was noted that all samples showed an increased absorbance at the 280 nm wavelength which indicates greater DNA presence in the sample.

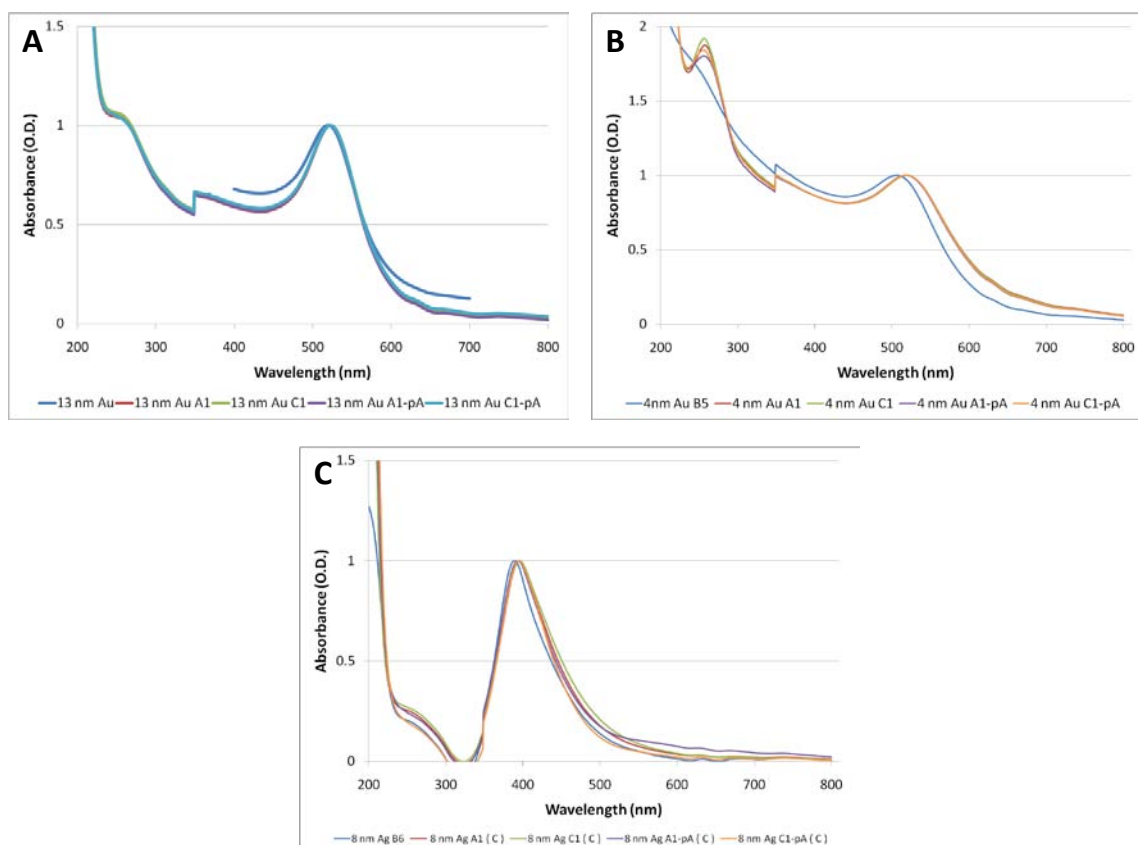


Figure 12. UV-Vis Absorption Spectra of Unfunctionalized and Functionalized Au and Ag NPs. (A) 13 nm Au NPs. (B) 4 nm Au NPs. (C) 8 nm Ag NPs.

To characterize the dehybridization temperature of the hybridized Au-DNA and Ag-DNA NPs, UV-Vis spectroscopy was performed on the sample by measuring the absorption at 280 nm while increasing the temperature of the sample. For the hybridized 13 nm Au-DNA NPs, the first set of NPs were hybridized in a 50 mM NaCl, 25 mM Tris Acetate (pH 8.2) solution, for which the dehybridization profiles are shown in Figure 13A. The effect of the poly-A sequence presence can be seen by the large shift in the dehybridization temperature (T_m), as well as the effect of hybridizing one complementary sequence without the poly-A to one containing the poly-A. In Figure 13A, the 13 nm Au A1+C1 NPs had the highest T_m point of the group at ~68 °C, followed by the 13 nm Au A1+C1-pA and C1+A1-pA NPs with an identical T_m of ~59 °C, and the 13 nm Au A1-pA+C1-pA NPs had the lowest T_m at ~40 °C. To observe the effects of salt concentration on dehybridization temperature, the same sets were hybridized in a 100 mM NaCl, 25 mM Tris Acetate (pH 8.2) and the results are shown in Figure 13B. All of the T_m 's shifted higher, with the 13 nm Au A1+C1 NPs shifting to ~74 °C, the 13 nm Au A1+C1-pA NPs shifting to ~63 °C, and the 13 nm Au A1-pA+C1-pA NPs increasing the most to ~52 °C. Visual images of the solutions pre- and post-melt are shown in Figure 13C, where the unique color shift of the NPs returns to the bright red color after dehybridizing indicating that they are individual NPs once again.

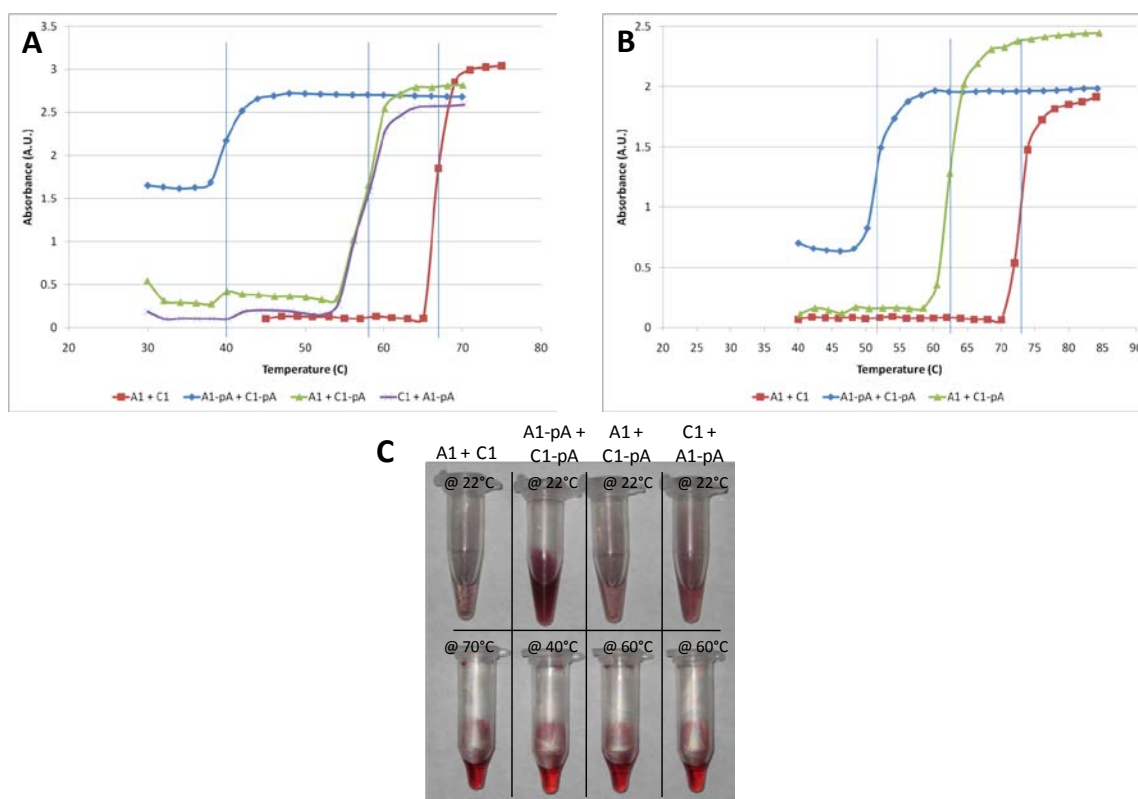


Figure 13. Dehybridization Curves for Hybridized 13 nm Au NPs. (A) Various hybridized 13 nm Au NPs in 50 mM NaCl buffer. (B) Various hybridized 13 nm Au NPs in 100 mM NaCl buffer. (C) Digital image of hybridized 13 nm Au NP solutions pre- and post-dehybridization.

The first trial of hybridizing the 4 nm Au-DNA NPs and 8 nm Au-DNA NPs in a 100 mM NaCl, 25 mM Tris Acetate (pH 8.2) solution was unsuccessful, evident by the results presented in Figure 14. The first indication that proper hybridization of the NPs did not occur was the lack of color shift of the hybridized (A1+C1) samples when compared to the single functionalized NPs (A1, C1) (Figure 14A). UV-Vis was performed to indicate if any hybridization had occurred, and as can be seen in Figure 14B, the data revealed that little to no hybridization had taken place.

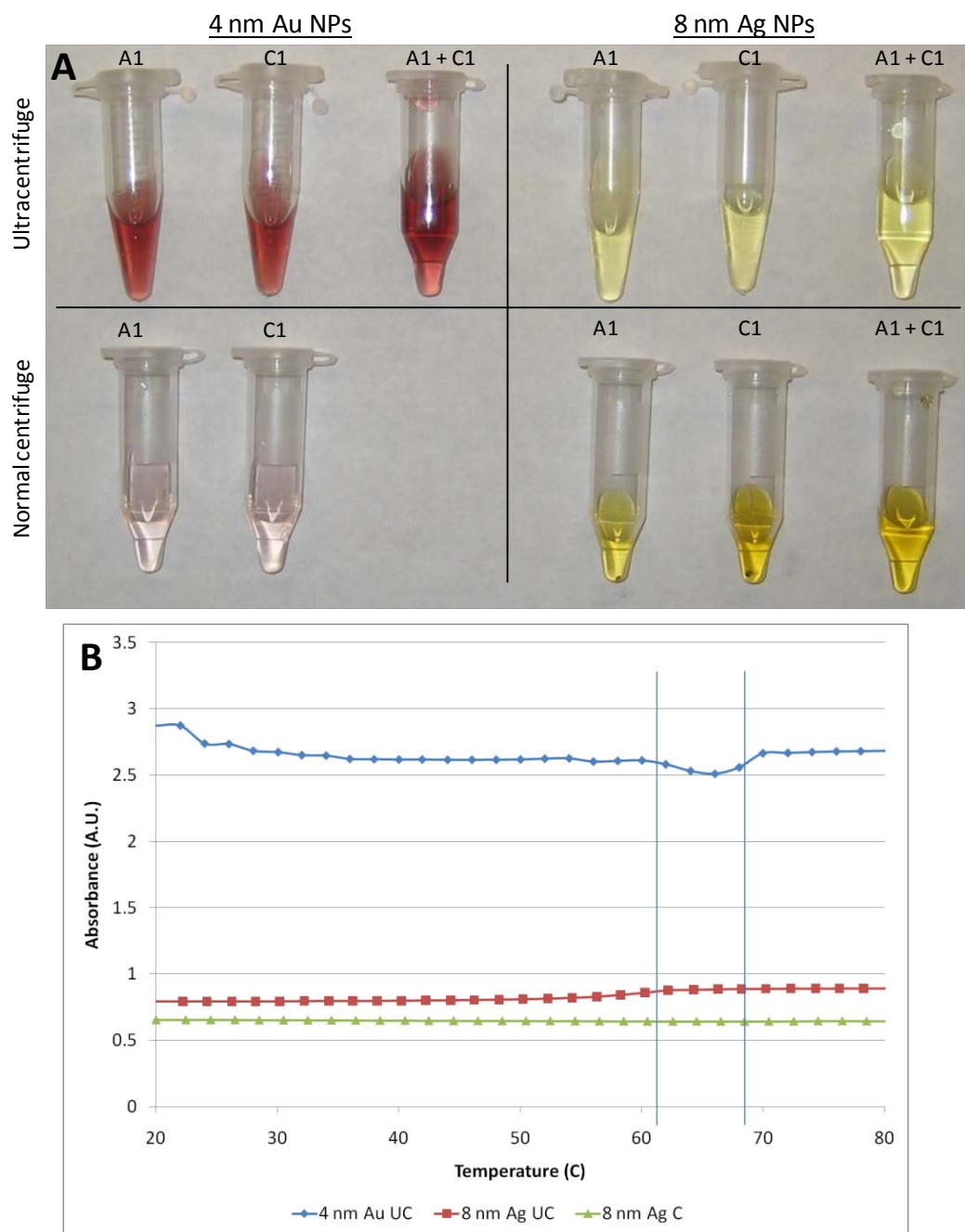


Figure 14. Functionalized and Hybridized 4 nm Au and 8 nm Ag NPs. (A) Digital images of the functionalized and hybridized solutions after standard centrifugation and ultracentrifugation. (B) Dehybridization curves for hybridized 4 nm Au and 8 nm Ag NPs.

After multiple modifications to the functionalization and hybridization procedures, the NP hybridization was attempted again with success with the results revealed in Figure 15. This time the color shift of the hybridized (A1+C1) samples is evident, initially indicating proper hybridization (Figures 15A and 15C). The hybridized 4 nm Au A1+C1 NPs exhibit a similar color shift as their larger counterparts; however both of the 8 nm Ag A1+C1 NPs samples have a

unique yellow to light orange color shift when hybridized (Figure 15C), but was more intense in the normal centrifuged sample due to larger NP sizes present. UV-Vis was performed on both NP types and both complementary sets of oligonucleotides to confirm proper hybridization by observing the dehybridization temperature. In Figure 15B, the dehybridization profiles for the 4 nm Au A1+C1 NPs, which were hybridized in a 300 mM NaCl, 25mM Tris Acetate (pH 8.2) solution, and 4nm Au A1-pA+C1-pA NPs, hybridized in a 500 mM NaCl, 25mM Tris Acetate (pH 8.2) solution, are represented with T_m 's of $\sim 79^\circ\text{C}$ and $\sim 71^\circ\text{C}$, respectively. The 8 nm Ag A1+C1 NPs (normal centrifuged sample), hybridized in a 300 mM NaCl, 25 mM Tris Acetate (pH 8.2) solution, had a T_m of $\sim 80^\circ\text{C}$ while the 8 nm Ag A1-pA+C1-pA NPs (normal centrifuged sample), hybridized in a 500 mM NaCl, 25 mM Tris Acetate (pH 8.2) solution, melted at $\sim 77^\circ\text{C}$ (Figure 15D). Even though the 2 ultra centrifuged samples, 8 nm Ag A1+C1 and 8 nm Ag A1-pA+C1-pA NPs, displayed a color change when hybridized, as seen in Figure 15C, they did not display a definitive dehybridization point when measured by UV-Vis.

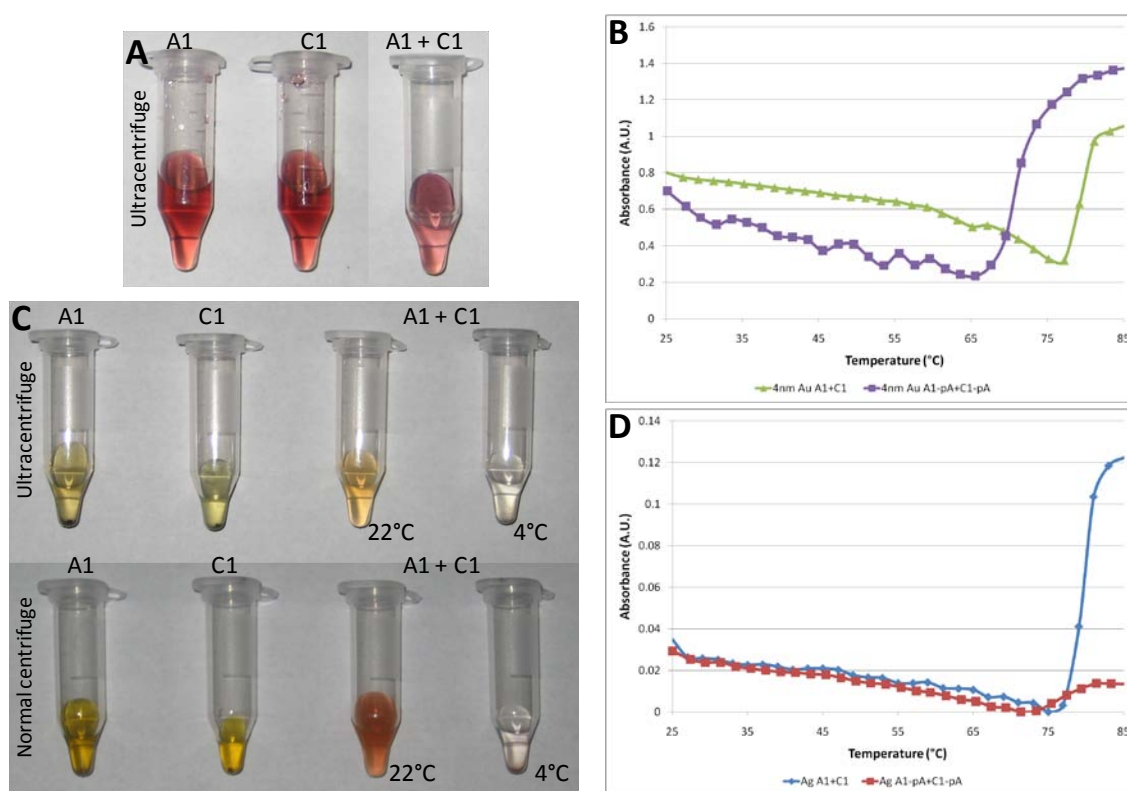


Figure 15. Functionalized and Hybridized 4 nm Au and 8 nm Ag NPs. (A) Digital images of the functionalized and hybridized 4 nm Au NPs after ultracentrifugation. (B) Dehybridization curves for hybridized 4 nm Au NPs. (C) Digital images of the functionalized and hybridized 8 nm Ag NPs after standard centrifugation and ultracentrifugation. (D) Dehybridization curves for hybridized 8 nm Ag NPs.

Hyperspectral Imaging. Hyperspectral Imaging (HSI) was performed on certain samples as a potential methodology for detecting NP state in a biological system in future studies. The HSI visual images and collected spectra are presented in Figure 16. The

unfunctionalized 13 nm Au NPs had a spectrum with a main peak at ~ 650 nm, with a slight secondary peak occurring at ~ 590 nm (Figures 16A and 16E). The 13 nm Au A1 NPs exhibited a peak scattering in the 610 nm to 630 nm wavelength range, with an overall narrower spectrum than the unfunctionalized NPs (Figures 16B and 16F). In Figure 16C, the large network formed by the hybridized 13 nm Au A1+C1 NPs can be easily seen, and the scattered spectra from this sample had a peak between 655 nm and 680 nm, with the narrowest overall spectra of the 13 nm Au NP samples (Figure 16G). The unfunctionalized and functionalized 4 nm Au NPs were too small to image using this system; however, a spectrum was collected from the hybridized 4 nm Au A1-pA+C1-pA NPs for comparison with a primary peak between 580 nm and 610 nm and a very slight secondary peak around 650 nm (Figures 16D and 16H).

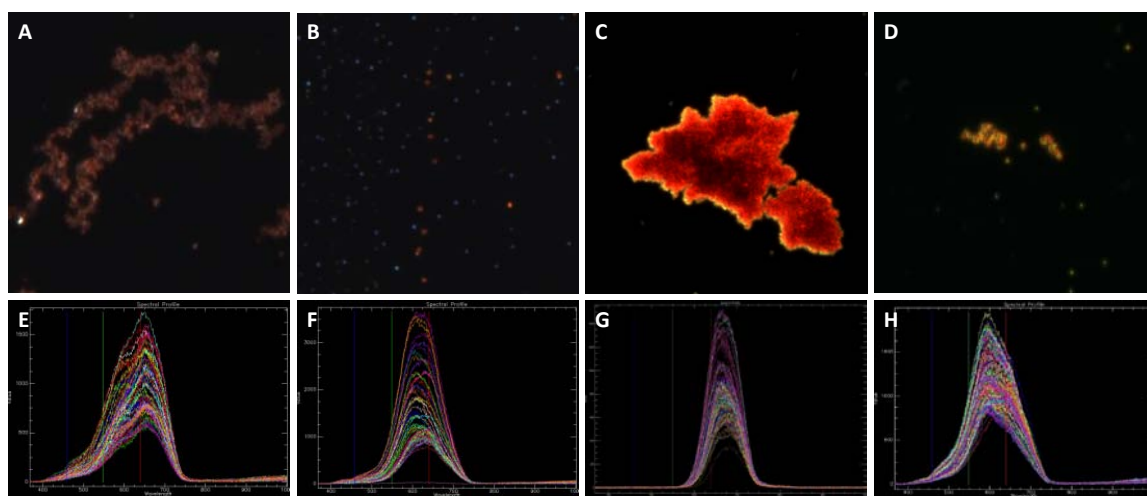


Figure 16. Hyperspectral Imaging of Unfunctionalized, Functionalized, and Hybridized Au NPs. (A) and (E) Digital image and spectra of 13 nm Au NPs. (B) and (F) Digital image and spectra of 13 nm Au A1 NPs. (C) and (G) Digital image and spectra of 13 nm Au A1+C1 NPs. (D) and (H) Digital image and spectra of 4 nm Au NPs.

Discussion

After synthesis of the NPs was completed, the next phase was to functionalize the NMs with biomolecules which would respond to heat changes near the surface of the NM. DNA was chosen for initial experiments because it is very stable in solution, even more stable when combined with NMs, can be easily obtained in customizable sequences, and double stranded DNA can be separated using thermal processes. Characterization was performed to verify that the primary NPs were not changing during the functionalization process, the DNA was being successfully attached to the NPs, and the DNA was still structurally intact and accessible after placement on the NP. DNA hybridization/dehybridization properties were also investigated. Images, TEM, UV-Vis, and DLS were all used in combination to verify one or more of these points. Visually, changes in NP aggregation in solution could be observed by changes in solution color, a unique property of plasmonic NPs and a significant reason Au and Ag NPs were chosen for this study^{35,40}. Successful NP hybridization can be visually observed in Figures 8A, 11C, 13A, and 13C; however, unsuccessful hybridization can be viewed in Figure 14A. TEM verified that all NPs were not significantly changed by the functionalization process, and also showed the characteristics of the hybridized NPs (Figures 10B, 10C, 10D, 11A, 11B, and 11C).

DLS verified the presence of the DNA on the surface of the NP by recording hydrodynamic diameter changes and also was used to help characterize hybridized samples (Table 2). UV-Vis was used to examine the attachment of the DNA to the surface of the NP (Figure 12), to determine relative molar concentrations of samples, and to characterize successful hybridization by examining the dehybridization temperatures of NP-DNA conjugates (Figures 11A, 11B, 13B, and 13D) or prove it to be unsuccessful (Figure 14B).

Functionalization of the colloidal Au and Ag was performed through thiol attachment of oligonucleotide sequences to the surface of the colloids. Two complementary sets of oligonucleotides, or single stranded DNA sequences, were chosen to perform preliminary functionalization and hybridization/dehybridization procedures in order to better characterize the impact on the DNA dehybridization temperature with changes in the surrounding environment. All DNA sequences contain a thiol modification at the 3' end of the sequence, which allows easy attachment of the DNA sequences to the surface of the Au and Ag NPs using a salt concentrating technique. The first set, A1 and C1, are 25-mer sequences which contain a 10-mer Poly A sequence to move the binding part of the oligonucleotide away from the surface of the NP, and the second set, A1-pA and C1-pA, have the same 15-mer binding sequence without the Poly A. This allowed observation of relative spacing of the hybridizing section from the surface of the NP and its effect on hybridization/dehybridization, which is important for future RF heating applications. The effect of the poly-A sequence was evident on all three NPs, where it was observed that the addition of the poly-A spacer increased the dehybridization temperature of the NPs, sometimes significantly, over the sequence without the poly-A spacer (Figures 11A, 11B, 13B, and 13D). For example, the A1+C1 complex melted at nearly 30°C higher than the A1-pA+C1-pA complex (Figure 13A). This increase can be attributed to the greater freedom of movement and flexibility exhibited with the poly-A spacer present while steric hindrances may be more prevalent when the poly-A spacer is not present. The data appears to be pointing to fact that this greater freedom of movement with the poly-A spacer would allow the DNA to withstand greater NP movement due to increased temperatures before being forced apart.

Some challenges were experienced when transitioning the functionalization procedure from the 13 nm Au NPs to the smaller 4 nm Au NPs and 8 nm Ag NPs. The main issues encountered were adjustment of the centrifugation washing process the NPs undergo, the initial DNA added to functionalize the NPs, and the salt concentrations required for hybridization. Centrifugation speeds used for the 13 nm Au NPs would not pellet the 4 nm Au NPs, and would only partially pellet the 8 nm Ag NPs. Hence, it was necessary to perform ultracentrifugation on the 4 nm Au NPs to successfully complete the washing procedures. As mentioned in the method section, the 8 nm Ag NPs contained a wider size distribution than Au NPs. Therefore, they were first centrifuged in a standard centrifuge to pellet larger NPs, and then the supernatant containing smaller NPs was transferred and ultracentrifuged. This produced 2 separate sets of functionalized NPs for the Ag sample. After the centrifugation processes were corrected, it was discovered that a significant amount of the NPs were not hybridizing in either the 4 nm Au NP or 8 nm Ag NP samples (Figure 14). At first it was thought that the initial concentration of the DNA sequences added to the bare NP solutions needed to be increased to increase coverage of each NP with DNA, since greater numbers of NPs were present in these samples. After doubling the initial DNA concentration for both samples and reattempting the functionalization and hybridization procedures, only 30-50% of the NPs were hybridizing in each of the samples. This indicated that the hybridizing salt concentration was not high enough to force the NPs to hybridize fully. The salt concentration was increased from 50 mM (Figure 14B) to 300 mM and

500 mM for the A1+C1 and A1-pA+C1-pA samples, respectively (Figure 15B and 15D), which corrected the issue.

Finally, hyperspectral imaging was performed to evaluate if the technology could be beneficial to this project when evaluating the state of the hybridized NPs when inside a biological system, both pre- and post-exposure to an RF signal. The technique was able to obtain scattering spectra from the 13 nm Au, 13 nm Au A1, and 13 nm Au A1+C1 NPs and show unique differences between their spectra. This would be useful for evaluating whether NPs were in the hybridized or dehybridized state inside a cell after RF exposure.

BIOCOMPATIBILITY OF NANOMATERIALS

Materials and Methods

HaCaT Cell Culture. Immortalized human keratinocytes (HaCaT cells) were used as a cellular model to determine the interaction of NPs with human skin. HaCaT cells were donated generously by Dr. James F. Dillman III, of the U.S. Army Medical Research Institute of Chemical Defense, 3100 Ricketts Point Road, Aberdeen Proving Ground, MD 21010-5400. The culture media for the HaCaT cells consisted of RPMI-1640 (ATCC) supplemented with 10 % fetal bovine serum (ATCC) and 1 % penicillin-streptomycin (Sigma). The cells are grown in 75 cm² vented flasks in a humidified incubator at a temperature of 37.0 °C and 5 % CO₂⁷⁴. The cells were passaged using 0.25 % trypsin with EDTA (GIBCO) when they reached 80% confluence and reseeded using a dilution ratio of 1:10.

PC-12 Cell Culture. Rat pheochromocytoma (PC-12) cells are a tumorigenic cell line from the adrenal gland and are used as endocrine and nervous cell models. PC-12 cells were obtained from ATCC (CRL-1721) in frozen form. PC-12 culture media consisted of F-12K media (ATCC) supplemented with 15 % horse serum (GIBCO), 2.5 % fetal bovine serum (ATCC), and 1 % penicillin-streptomycin (Sigma). The cells were grown in 75 cm² vented flasks in a humidified incubator at a temperature of 37.0 °C and 5% CO₂⁷⁵. The cells were passaged using 0.25 % trypsin with EDTA when they reached 80 % confluence and reseeded using a dilution ratio of 1:10.

Biocompatibility Assessment

Nanoparticle Dosing Solutions. Dosing solutions of the unfunctionalized 4 nm Au NPs and 8 nm Ag NPs were made in either the PC-12 cells or HaCaT cells culture media at molar particle concentrations of 1, 2.5, 5, and 10 nM, as determined by UV-Vis spectroscopy (Section II, page 26). For the 13 nm Au and 13 nm Au-DNA NPs, a dosing concentration of 2.5 nM was used.

Cell Viability. Cell viability was assayed using the CellTiter 96[®] AQueous One Solution Cell Proliferation Assay (Promega). This assay is a colorimetric method used to determine the number of viable cells in proliferation or cytotoxicity experiments. MTS (3-(4,5-dimethylthiazol-2-yl)-5-(3-carboxymethoxyphenyl)-2-(4-sulfophenyl)-2H-tetrazolium), in the presence of phenazine methosulfate (PMS), produces a water-soluble formazan salt that has an absorbance maximum at 490-500 nm in phosphate-buffered saline. The CellTiter 96[®] AQueous One Solution Reagent contains MTS and an electron coupling reagent (phenazine ethosulfate; PES), which has enhanced chemical stability and allows it to be combined with MTS to form a stable, single solution.

HaCaT cells were seeded at 30,000 cells/cm² and the PC-12 cells were seeded at 40,000 cells/cm² in a 96-well, flat bottom culture plate with 200 µL per well. The cells were grown for 24 h in a humidified, 5% CO₂ incubator at 37 °C until ~80% confluent. Existing media was aspirated and 200 µL of the dosing solutions were added to the wells. The cultures were incubated for an additional 24 h, at which point the dosing solutions were aspirated, and the cells

were washed three times with 100 μ L of 1X phosphate buffered saline solution (PBS). Next, 100 μ L of complete culture media and 20 μ L of the CellTiter 96® AQueous One reagent was added to each well, and then incubated for 1 h at 37 °C. The plates were then placed on a plate stirrer for a few minutes to evenly distribute the MTS product in each solution for consistent measurements. Plates were measured using a BioTek Synergy HT spectrophotometer with GenX 5 software for sample absorbance at a wavelength of 490 nm. The relative cell viability (%) of the NP dosed wells as compared to control wells was calculated by $[A]_{\text{test}} / [A]_{\text{control}} \times 100$. Where $[A]_{\text{test}}$ is the absorbance of the test sample and $[A]_{\text{control}}$ is the absorbance of control sample. Each experiment was performed in triplicate, and the data are represented as the mean \pm standard deviation with $n \geq 25$ for each sample. Statistics were run on the data using a one-way ANOVA test in JMP 7.0 software from SAS.

Cell Morphology and Nanomaterial Interaction. The CytoViva Ultra-Resolution Imaging (URI) microscope was used to examine the cell-NP interactions and to observe any change in cell morphology. HaCaT cells and PC-12 cells were plated in dual chambered slides at cell densities of 30,000 cells/cm² and 40,000 cells/cm², respectively. After a 24 h incubation, the media was aspirated and the cells were dosed at 2.5 nM, for both the 4 nm Au NPs and 8 nm Ag NPs in complete media. After a 24 h exposure, the media was removed, and the cells were fixed in 1 mL of 4% paraformaldehyde in PBS for 10 min at room temperature. The cells were then rinsed once with PBS, then incubated with 25 μ L/mL of the AlexaFluor 555-Phalloidin (actin) and 1 μ L/mL of the Hoescht (nuclear) stains for 1 h at 37 °C. The cells were then rinsed 3 times with PBS, and the chambers were removed from the slides. A 10 μ L drop of PBS was added to each sample square and then a cover slip was placed over each sample and sealed with clear nail polish. After the nail polish had dried, the samples were imaged using the CytoViva URI microscope⁷⁶.

Nanomaterial Uptake. To evaluate the uptake of the NPs into the cells, treated cells were sectioned and imaged under TEM. A modified procedure of the method published by Schrand, et al. (2010) was used⁷⁷. HaCaT cells were seeded at 30,000 cells/cm² (2 mL volume/well) into a flat-bottom, 6-well cell culture plate and incubated at 37 °C for 24 h. The media was aspirated from each well, and 2 mL of 2.5 nM dosing solutions of 4 nm Au NPs in complete media was added to 4 wells. Media without NPs was added to 2 wells (control samples). After a 24 h exposure, the media was aspirated, and 1 mL of 0.25 % trypsin with EDTA was added to each well and incubated at 37°C for 5 min to detach the cells from the bottom of the plate. Each cell solution was then transferred to a 15 mL conical tube and 5 mL of complete media was added to each sample. The cells were centrifuged for 10 min at 800 x g. The supernatant was removed, and the cell pellets were transferred to conical-tipped embedding capsules (BEEM, EMS). Next, 500 μ L of 2% paraformaldehyde (diluted with PBS) was added to each pellet and fixed overnight at 4 °C. The paraformaldehyde solution was removed, and the pellet was rinsed 3 times for 30 min each with 1X PBS. Cell pellets were stained using 300 μ L of 1% osmium tetroxide (OsO₄) (EMS), which was diluted in PBS, for 1 h. The OsO₄ was removed from each pellet and neutralized in corn oil. From this point forward, all waste solution was added to corn oil to neutralize any remaining OsO₄. Cell pellets were rinsed with PBS 3 times for 10 min each to remove remaining OsO₄. Next, the pellets were dehydrated using decreasing ethanol (EtOH) dilutions prepared in water. First, 300 μ L of 50 % EtOH was added to each pellet for 10 min. The solution was removed and 300 μ L of 70 % EtOH was added 3

times for 10 min each, removing the solution each time. Next, 300 μ L of 80 % EtOH was added to each pellet for 10 min, followed by removal of the solution and addition of 300 μ L of 90 % EtOH 10 min. The previous solution was removed, and 300 μ L of 100 % EtOH was added 3 times for 10 min each, with removal of the solution after each time period. Finally, 300 μ L of a 1:1 dilution of 100 % EtOH and LR White resin (EMS) was added to each sample for 1 h. The embedding capsule was then filled the rest of the way with resin, and the samples were placed in a vacuum oven overnight at 60 °C to cure.

Ultramicrotome sectioning of the samples was performed according the procedure described by Schrand et al. (2010) on a Leica EM UC7 ultramicrotome using an Ultra 45° diamond knife (DiATOME). Sections were placed on 200 mesh, formvar/carbon-coated copper grids and imaged using a Hitachi H-7600 tungsten-tip instrument at an accelerating voltage of 100 kV in high contrast mode.

Hyperspectral Imaging. HaCaT cells were plated in dual chambered slides at cell densities of 30,000 cells/cm² and incubated for 24 h. The media was aspirated and the cells were dosed with 13 nm Au A1-pA+C1-pA at a concentration of 2.5 nM in complete media for an additional 24 h. The control cells were not dosed, but did undergo a media change at the same timepoint as the treated cells. The media was removed and the cells were fixed in 1 mL of 4% paraformaldehyde in PBS for 10 mins at room temperature. The cells were then rinsed 3 times with PBS, and then the chambers were removed from the slides. A 10 μ L drop of PBS was added to each sample square and then a cover slip was placed over each sample and sealed with clear nail polish. After the nail polish had dried, the samples were scanned on the CytoViva Hyperspectral Imaging System (HSI). Scan information and spectra were collected and processed through the ENVI software.

Results

Biocompatibility. Cell viability (MTS) was assessed for the unfunctionalized 4 nm Au and 8 nm Ag NPs. For the HaCaT cells exposed to the 4 nm Au NPs, statistically significant stimulatory effects were seen at the 2.5 and 5 nM concentrations, with viability increasing ~20 % above control for both exposures (Figure 17). All concentrations of the 8 nm Ag NPs produced a statistically significant increase in HaCaT viability at 18 % (1 nM), 30 % (2.5 nM), 45 % (5 nM), and 30 % (10 nM) greater than control cells (Figure 17).

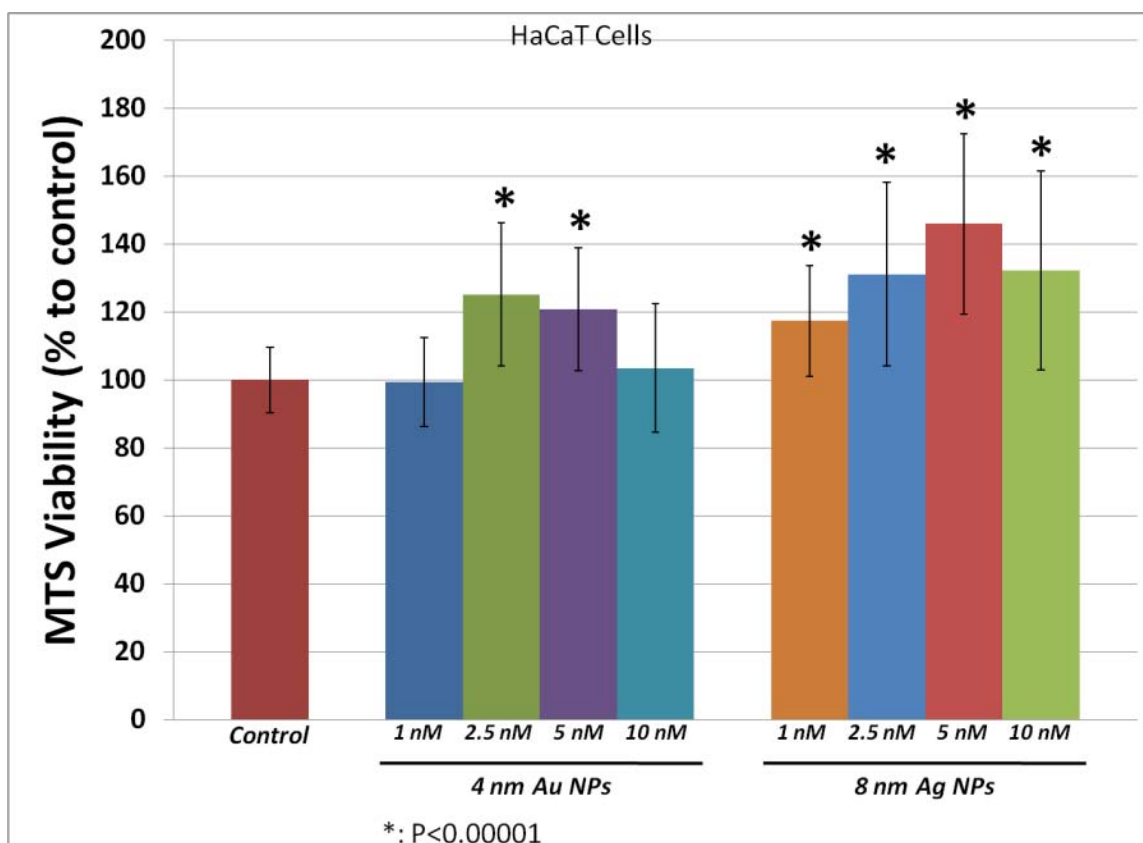


Figure 17. Biocompatibility of Unfunctionalized 4 nm Au NPs and 8 nm Ag NPs in HaCaT cells.

Control of Cellular Signaling. Future studies will include attempting to remotely control cellular signaling using the biofunctionalized NPs under RF stimulation. The PC-12 cells are an excellent candidate for these studies as their growth and differentiation signaling pathways have been well defined⁷⁵. Depending on the transient or sustained activity of ERK in the pathway, a proliferative response can be attained, similar to the EGF response in the cell, or a differentiation response, similar to the NGF response. Cell viability was assessed for the unfunctionalized, functionalized, and hybridized 13 nm Au NPs (Figure 18). For the 13 nm Au NPs, the only sample which displayed a significant impact on PC-12 cell viability was the 13 nm Au A1 NP sample, which decreased viability slightly, to ~81 % as compared to control cells (Figure 18). Similar stimulatory effects were seen with the treated PC-12 cells, as in the HaCaT cells, for both the unfunctionalized 4 nm Au and 8 nm Ag NPs. The PC-12 cells dosed with the 4 nm Au NPs exhibited statistically significant increases in viability at 1, 2.5, and 5 nM concentrations with increases of 10 %, 19 %, and 18 %, respectively. The 10 nM treatment returned to control levels (Figure 19). The 8 nm Ag NP treated PC-12 cells followed a similar trend as the HaCaT cells by showing statistically significant viability increases ~20-25 % for the 1, 2.5, and 5 nM treatments (Figure 19). However, the highest Ag treatment, 10 nM, exhibited decreased viability at ~83 % and was significantly different from the control (Figure 19).

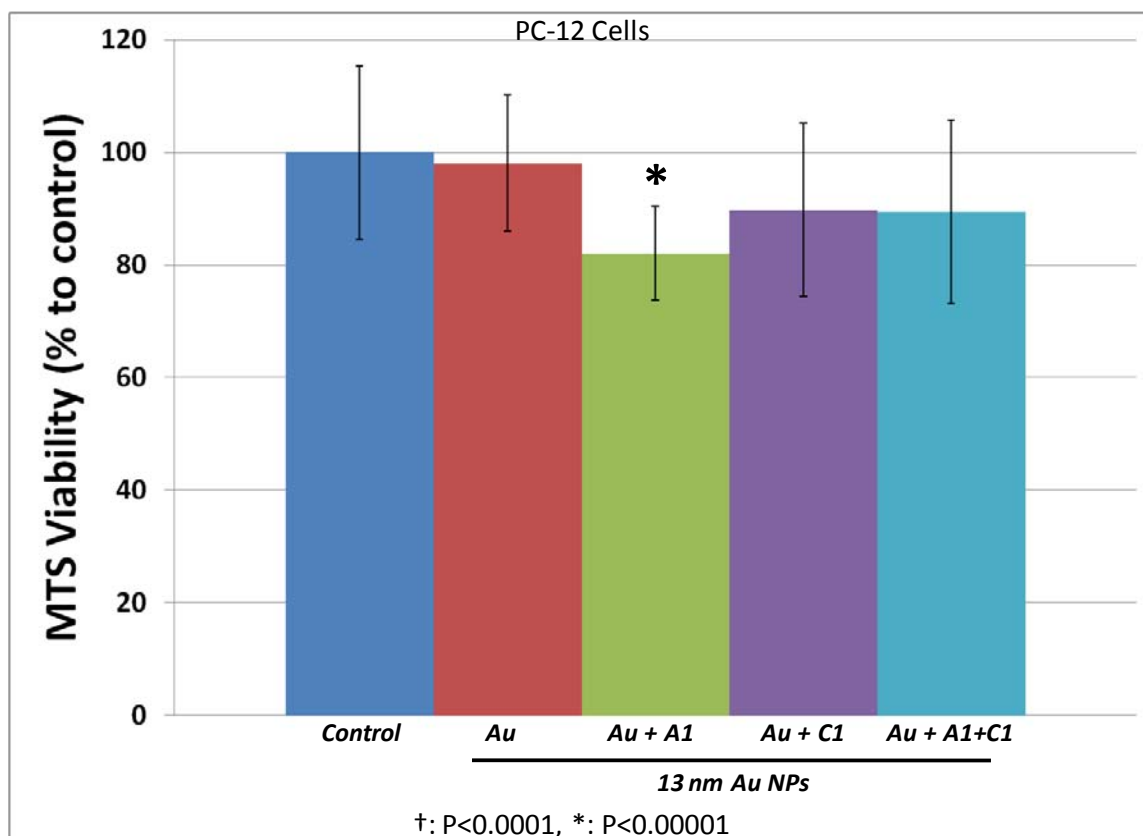


Figure 18. Biocompatibility of Unfunctionalized, Functionalized, and Hybridized 13 nm Au NPs in PC-12 Cells.

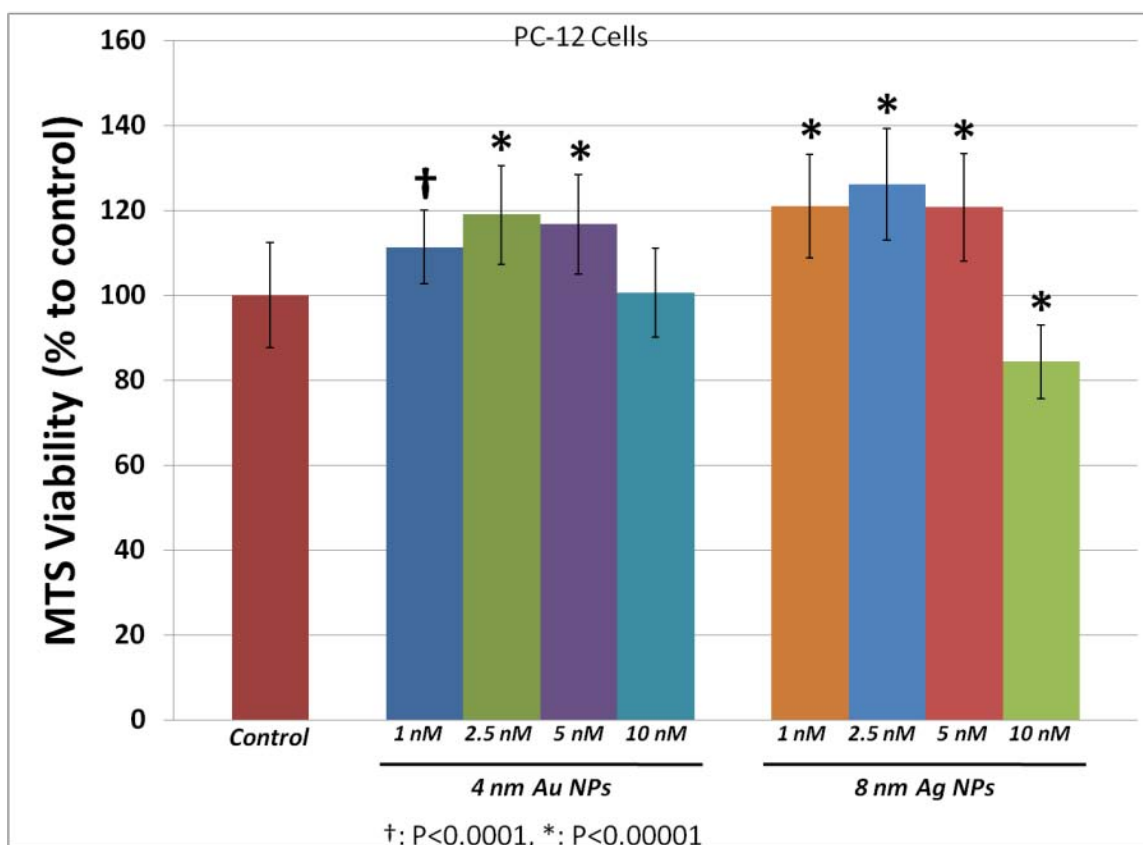


Figure 19. Biocompatibility of Unfunctionalized 4 nm Au NPs and 8 nm Ag NPs in PC-12 Cells.

Cell Morphology and Nanomaterial Interaction. In addition to cell viability, cell-NP interactions and cell morphology were assessed. The unfunctionalized 4 nm Au NPs appeared to accumulate at cell-cell junctions in the HaCaT cells as well as randomly in the cytoplasm (Figure 20A, red arrows). However, in the PC-12 cells the 4 nm Au NPs appear to be mainly internalized in larger aggregates, potentially encapsulated in lysosomes or other membrane bound organelles, as indicated by the larger, brighter spots seen inside the cytoplasm (Figure 20C). The majority of the 8 nm Ag NPs interacting with the HaCaT cells appear to be localized in the cytoplasm and in close proximity to the nuclei (Figure 20B), with similar results in the PC-12 cells except the aggregates in the cytoplasm appeared to be larger (Figure 20D).

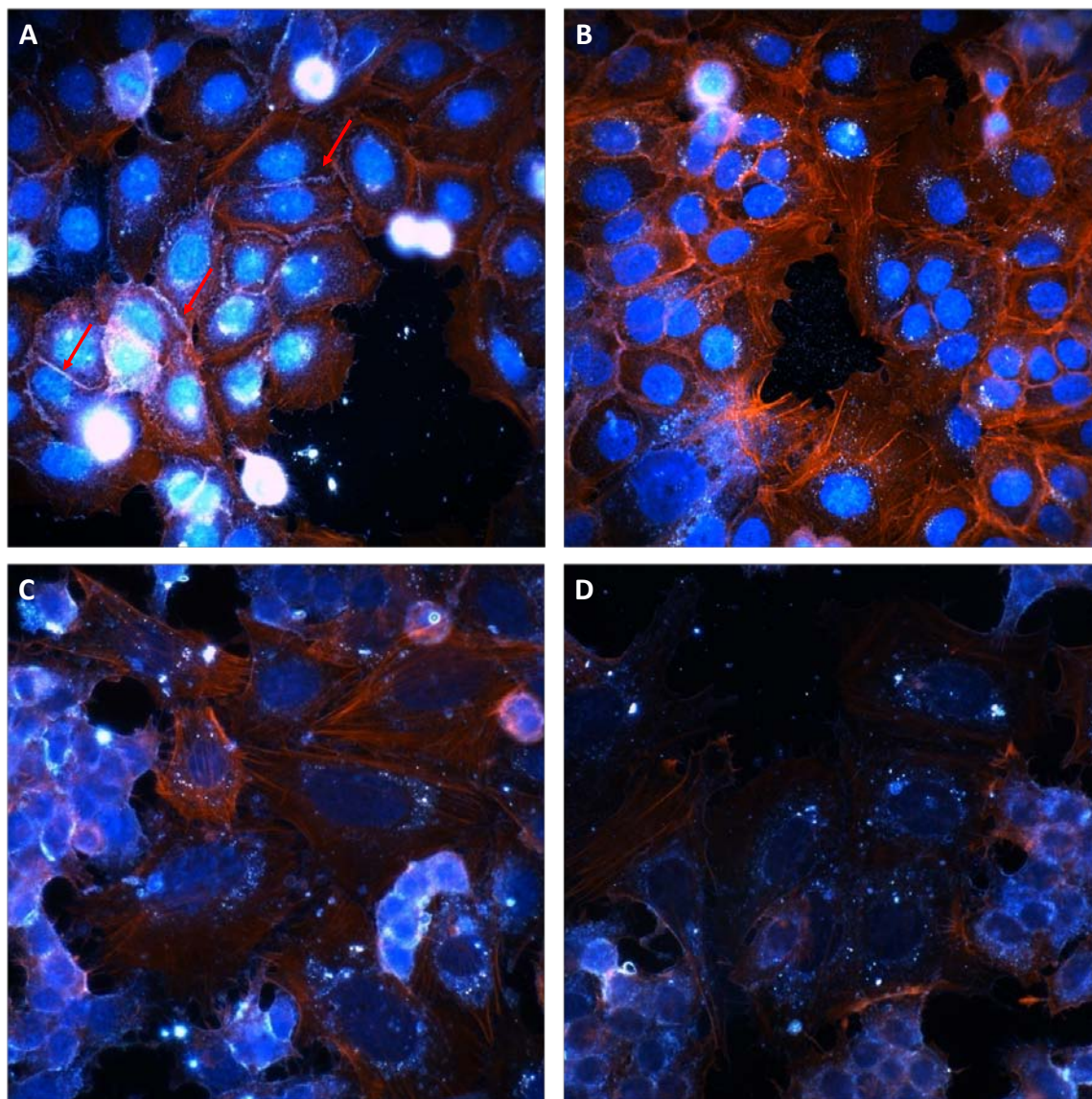


Figure 20. CytoViva URI Images of HaCaT Cells and PC-12 Cells Treated with Unfunctionalized 4 nm Au and 8 nm Ag NPs. (A) HaCaT cells treated with 4 nm Au NPs. (B) HaCaT cells treated with 8 nm Ag NPs. (C) PC-12 cells treated with 4 nm Au NPs. (D) PC-12 cells treated with 8 nm Ag NPs.

Nanomaterial Uptake. To verify the uptake which appeared to be occurring in the CytoViva images in Figure 20, TEM imaging was performed to confirm localization of NPs within the cells. HaCaT cells were treated with unfunctionalized 4 nm Au NPs and then prepared for TEM studies as described in the methods section. Figures 21A and 21B show a large aggregate of NPs in the cytoplasm encased in a membrane-bound vacuole, possibly an endosome or lysosome. Upon further magnification, the NPs appear to be intact and have not significantly changed in morphology (Figure 21C). Also in Figure 21A, other smaller aggregates of NPs are present in the cytoplasm, and a much smaller group was observed to be located freely in the cytoplasm (not contained in a vacuole). It was also observed that some very large

aggregates appeared to not be contained by a vacuole and had been assimilated into the cytoplasm (Figure 22). In Figures 22B and 22C, it can be seen that the aggregate appears to have localized near a folded cellular structure, possibly the endoplasmic reticulum or Golgi body. Even with a large amount of NPs localizing within the cells, no abnormal cell morphologies or structures were observed (Figure 22A).

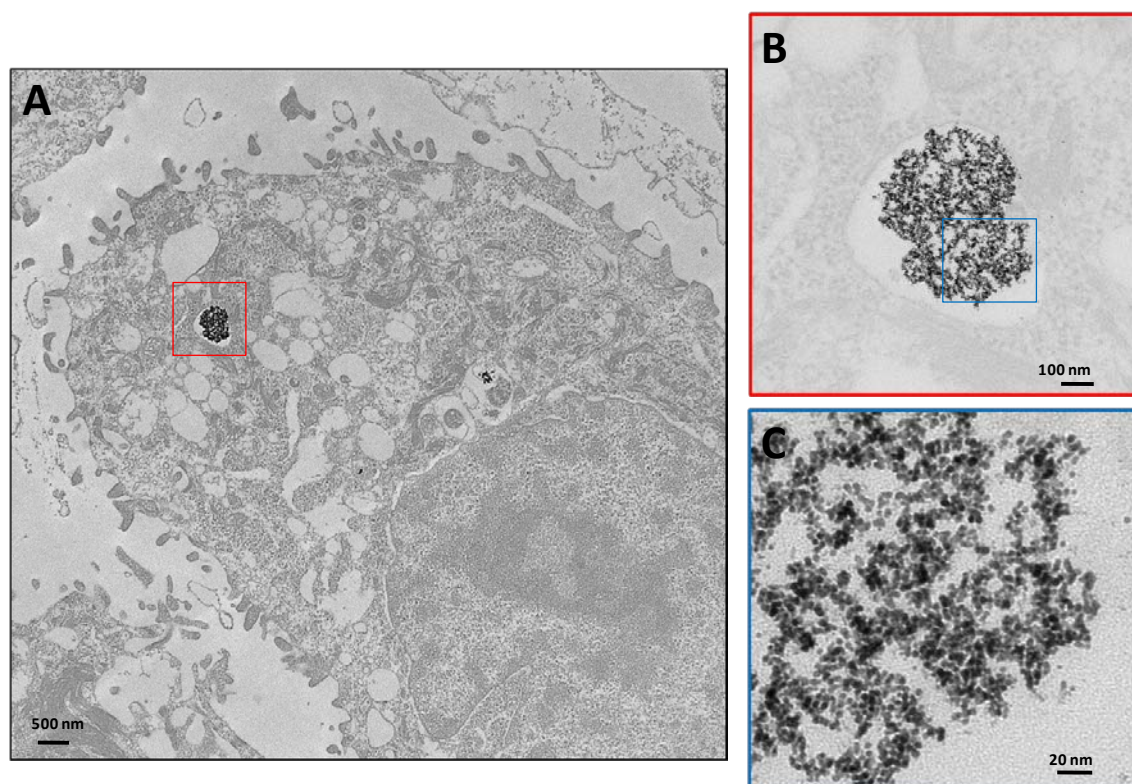


Figure 21. Uptake of Unfunctionalized 4 nm Au NPs into HaCaT Cells. Area imaged in (B) is zoomed area of red outlined area in (A). Area imaged in (C) is zoomed area of blue outlined area in (B).

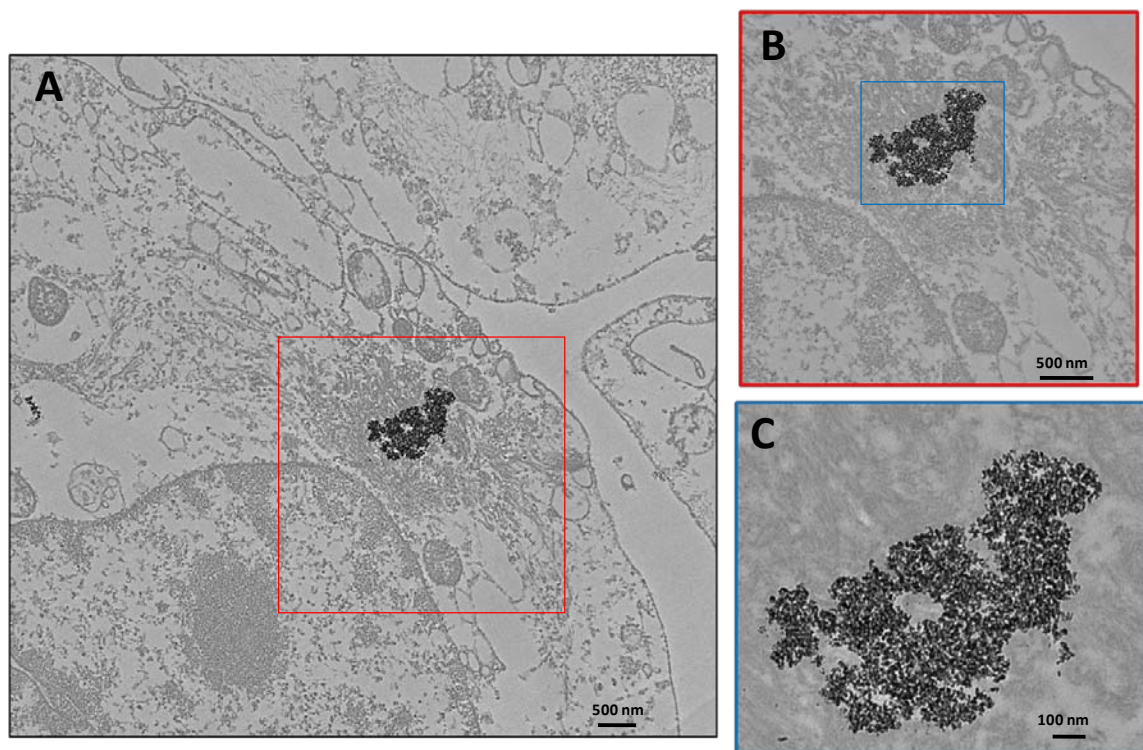


Figure 22. Uptake of Unfunctionalized 4 nm Au NPs into HaCaT Cells. Area imaged in (B) is zoomed area of red outlined area in (A). Area imaged in (C) is zoomed area of blue outlined area in (B).

Hyperspectral Imaging. HSI was used now to evaluate if the spectral signature that was obtained for the hybridized NPs in the previous section, could still be observed once the NPs were placed in a cellular environment and even taken into a cell. In Figure 23A, HaCaT control cells were scanned to provide a baseline, or background, spectrum to compare with the treated cells (Figure 23C). The HaCaT cells treated with 13 nm Au A1-pA+C1-pA NPs were scanned and the Au-DNA aggregates can be seen localizing around the cells and potentially inside the cells (Figure 23B). The spectra produced appeared to be a combination of the cell and the Au-DNA spectra (Figure 23D). The characteristic peak for the 13 nm Au-DNA NPs was observed at 650-680 nm, with the cell spectrum appearing to cause the broadening of the peak into the green wavelengths (Figure 23D).

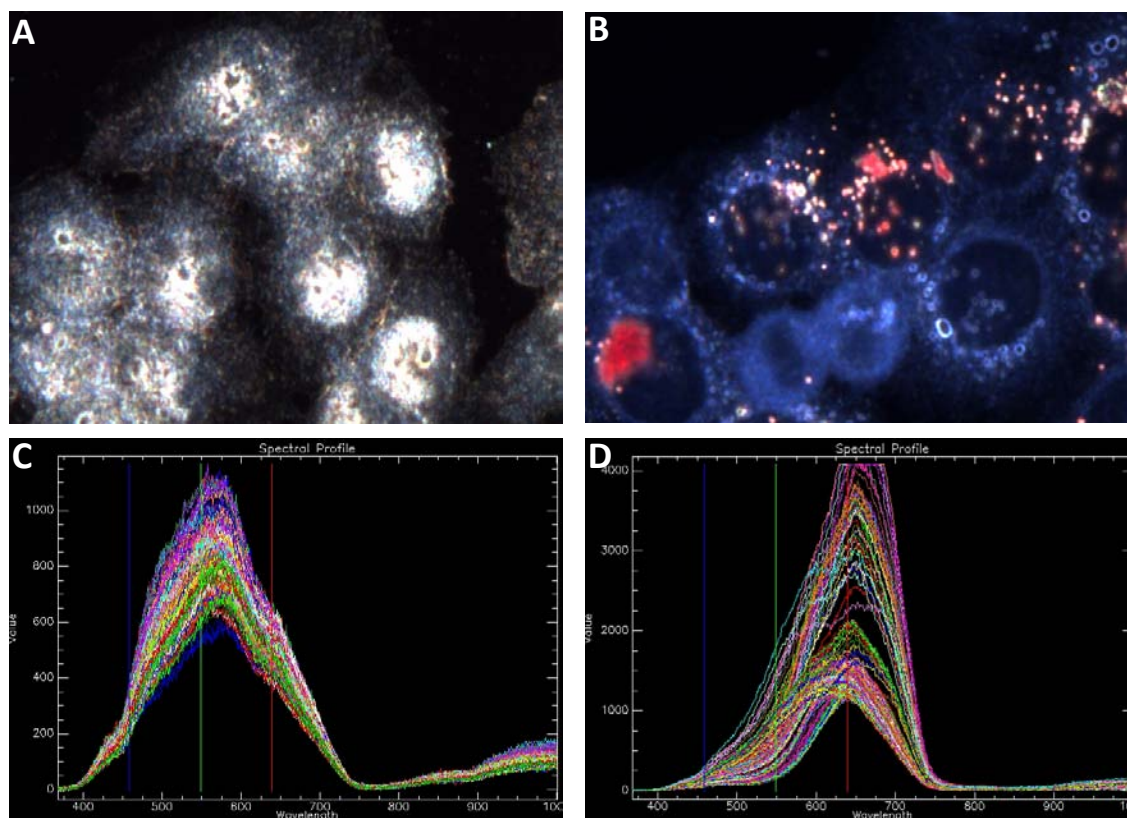


Figure 23. Hyperspectral Imaging of Untreated HaCaT Cells and HaCaT Cells Treated with Hybridized 13 nm Au NPs. (A) and (C) Digital image and background spectra of untreated HaCaT cells. (B) and (D) Digital image and spectra of 13 nm Au A1-pA+C1-pA NPs.

Discussion

Biocompatibility assessment of the unfunctionalized 13 nm and 4 nm Au NPs, as well as the 8 nm Ag NPs, was performed using HaCaT (human keratinocytes) and PC-12 (rat adrenal gland) cells after an exposure of 24 h. After triplicate experiments, it was observed that at all concentrations tested, except one, there were no detrimental effects from the 4 nm Au and 8 nm Ag NPs; however, a stimulatory effect was seen at most concentrations (Figures 17 and 19). The only detrimental effect observed was at the highest concentration tested of the 8 nm Ag NPs in the PC-12 cells (Figure 19). Biocompatibility assessment of oligonucleotide-coated 13 nm Au NPs was performed with the PC-12 cell line with only a slight decrease in viability seen with the functionalized (unhybridized) NPs (Figure 18). Cell morphology and uptake of the NPs were also observed. No significant changes to cell morphology were seen; however, the stimulatory effect observed in the MTS assays was evident as the 4 nm Au NP treated cells exhibited approximately 30 % more cells at 24 h when compared to control cells.

Uptake of large aggregates of the unfunctionalized 4 nm Au NPs was seen in HaCaT cells, indicating that uptake of large NP-DNA conjugates is possible and that they could remain intact for at least 24 h (Figures 21 and 22). Also, since they would remain in conjugated form, this would limit their action inside the cell until stimulated and released by RF exposure. It also appears that in Figure 22, the aggregate of NPs appears to be localized near the endoplasmic reticulum or Golgi body; however, further immunological staining would need to be conducted

to confirm this. If this is the case, it raises an interesting question of how the large aggregate of NPs was taken into the cell and was not, or no longer was, packaged in an endosome especially since the NPs were not specifically functionalized with a biomolecule to aid in localization inside the cell.

The HSI data showed promising results of detecting the hybridization state of the NPs while localized near or inside the cells (Figure 23). The combined signal of the cell background and the hybridized NPs can be separated using spectral unmixing techniques to help improve NP spectral identification (Figure 23D). Also, multiple aggregates can be seen in many of the cells' cytoplasm, indicating uptake of the hybridized NPs, but this would need to be verified with ultramicrotome sectioning and TEM imaging (Figure 23B).

RADIO FREQUENCY HEATING OF NANOMATERIALS

Materials and Methods

Radio Frequency (RF) Exposure System. The RF exposure system used for this experiment was located at the University of Kentucky and was accessed through Dr. Zach Hilt. The system operated at a frequency of 13.56 MHz with an adjustable power output between ~10 W to 500 W. The RF generator / power amplifier (Cesar 136, Advanced Energy, P/N 61300047) was connected through a Type-N cable to a variable matching network (VarioMatch 600, Advanced Energy, P/N 69000020), which matched the impedance of the power amplifier signal to the water cooled, solenoid antenna. The solenoid antenna, made of 7/16" hollow copper tubing, was ~3" in diameter, with 4 turns and 1/2" spacing between turns.

To expose the NM solutions, 500 μ L of each sample tested was placed into a 1 cm x 1 cm polystyrene cuvette, which had been trimmed to ~1 cm tall and positioned on a Teflon block very close to the outer edge of the coil. An example of the exposure arrangement can be seen in Figure 25D. Each sample was exposed to the RF signal at an amplifier setting of 400 W for 180 s. The 180 s exposure time was experimentally determined to be optimal to stay within the calibrated temperature range of the IR camera. Temperature change of the solution was measured over time by an infrared camera (FLIR SC4000) and recorded by FLIR camera software at a rate of 1 frame per second.

Calculation of Nanomaterial Heating Properties. The power generation, in relation to various NP properties, was calculated from the solution heating curves obtained for each unfunctionalized NP. The total energy transfer to the solution from the NPs was calculated using the heat capacity formula:

$$Q = mc(T(t_f) - T(t_0))$$

where m is the mass in g of sample, c is the specific heat capacity in J/g·K, $T(t_0)$ is the initial solution temperature in K, and $T(t_f)$ is the temperature of each NP solution in K after 70 s of RF exposure. The heat transfer was converted to average power (W) and expressed relative to calculated values for W/particle, W/nm², and W/nm³. An example calculation of the particle properties is shown in Appendix A, page 94 and the particle power generation is shown in Appendix B, page 96.

Results

Radio Frequency Heating of Nanomaterials. RF heating measurements of unfunctionalized Au and Ag NPs in solution are presented in Figure 24. The 4 nm Au and 8 nm Ag NPs were exposed to the RF signal and significant heating was observed in both samples, with increases of 50 °C and 45 °C, respectively, over 180 s (Figures 24A, 24B, and 24D). To verify the heating was a result of the NPs being present, DI H₂O and metal precursor solutions used for NP synthesis were tested as negative controls. The DI H₂O exhibited no heating, and the metal precursor solutions exhibited a 12 °C and 15 °C increase for the HAuCl₄ solution and AgNO₃ solution, respectively (Figure 24A).

Due to heating differences observed between functionalized NPs in NaCl solutions and unfunctionalized NPs in DI H₂O, which are discussed later and the results presented in Figure 25, the same concentrations of each NPs were dispersed in salt solutions as well to record any difference in heating. A visible color shift in the solution occurred for each NP when dispersed in the salt solutions, indicating aggregation of the NPs; however, no visible precipitates were

formed. In Figure 24B, the heating of the 4 nm Au NPs dispersed in 300 mM NaCl solution was drastically less than the water dispersed sample at 3 °C. This significantly reduced heating of the NPs in salt solutions was also observed for the 13 nm Au NPs (50 mM NaCl) and the 8 nm Ag NPs (300 mM NaCl), which reduced to 12 °C and 5 °C, respectively, after 180 s (Figures 24C and 24D).

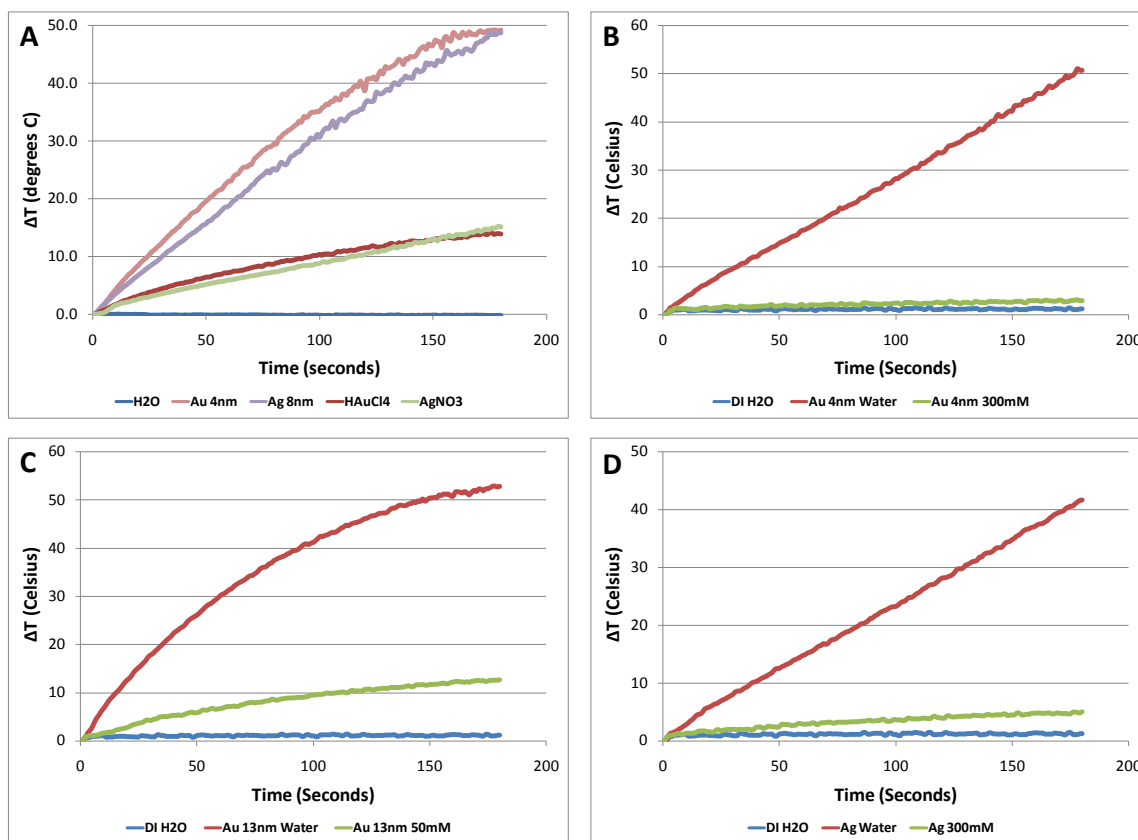


Figure 24. RF Heating Curves of Unfunctionalized Au and Ag NPs in Water and Hybridization Buffer. (A) Heating of 4 nm Au NPs in water, 8 nm Ag NPs in water, HAuCl₄ solution, and AgNO₃ solution. (B) 4 nm Au NPs in water and 300 mM NaCl solution. (C) 13 nm Au NPs in water and 50mM NaCl solution. (D) 8 nm Ag NPs in water and 300 mM NaCl solution.

Unfunctionalized, functionalized, and hybridized NPs were diluted to equivalent total volume of particles ($3 \times 10^{13} \text{ nm}^3$) to determine whether the heating is a volumetric effect as previously theorized⁵⁰. When diluted to equivalent total particle volumes, the total number of particles and total surface area were different for each sample, as shown in Table 3. When the volume is held constant, surface area and particle number increase as NP diameter decreases. These results will be used to compare NP heating between each sample.

Table 3. Differences in NP Sample Physical Characteristics When Dispersed at Equal Total Volume Concentrations.

Sample	Volume (nm³)	Surface Area (nm²)	Number of Particles
<i>Au 13 nm</i>	3.000E+13	1.385E+13	2.608E+10
<i>Au 4 nm</i>	3.000E+13	4.500E+13	8.952E+11
<i>Ag 10 nm</i>	3.000E+13	2.250E+13	1.119E+11

The heating results of the equivalent volume diluted samples are shown in Figure 25. For the functionalized NP and the hybridized NP samples, each were exposed in the hybridization buffer which was deemed optimal from the functionalization trials presented in Section III, page 35. The unfunctionalized NPs were dispersed at the same volume concentration in the hybridization buffer as well to compare heating. The unfunctionalized 4 nm Au NPs in water did not show any significant heating above the water only sample when exposed to RF (Figure 25A). The unfunctionalized 4 nm Au NPs, the 4 nm Au A1 NPs, and the 4 nm Au A1+C1 NPs, all being dispersed in 300 mM NaCl solution, increased ~4 °C after 180 s of RF exposure (Figure 25A). The 13 nm Au samples exhibited similar heating to the 4 nm Au samples, except the unfunctionalized 13 nm Au NPs increased by ~2 °C, when compared to water only observations (Figure 25B). However, the unfunctionalized 4 nm Au NPs and the 4 nm Au A1 NPs dispersed in 50 mM NaCl solutions, increased ~14 °C. Also, the 4 nm Au A1+C1 NPs, also dispersed in 50 mM NaCl solution, increased ~12 °C (Figure 25B). The 8 nm Ag NP samples were opposite in trend from both of the Au NPs. The unfunctionalized 8 nm Ag NPs dispersed in water increased ~11 °C, while the unfunctionalized 8 nm Ag NPs, 8 nm Ag A1 NPs, and the Ag A1+C1 NPs, all dispersed in 300 mM NaCl solution, increased ~3 to 3.5 °C (Figure 25C).

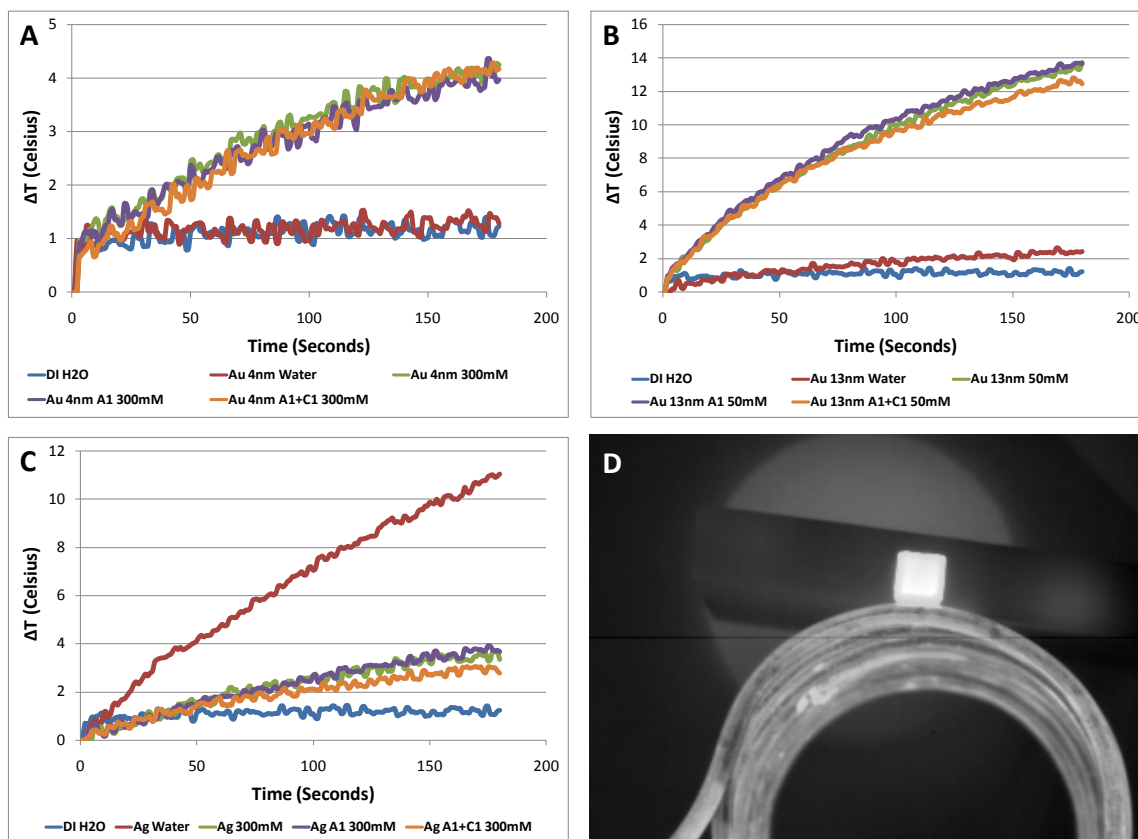


Figure 25. RF Heating Curves of Unfunctionalized, Functionalized, and Hybridized Au and Ag NPs. (A) 4 nm Au NPs in water, 4 nm Au NPs in 300 mM NaCl solution, 4 nm Au A1 NPs in 300 mM NaCl solution, and 4 nm Au A1+C1 NPs in 300 mM NaCl solution. (B) 13 nm Au NPs in water, 13 nm Au NPs in 50 mM NaCl solution, 13 nm Au A1 NPs in 50 mM NaCl solution, and 13 nm Au A1+C1 NPs in 50 mM NaCl solution. (C) 8 nm Ag NPs in water, 8 nm Ag NPs in 300 mM NaCl solution, 8 nm Ag A1 NPs in 300 mM NaCl solution, and 8 nm Ag A1+C1 NPs in 300 mM NaCl solution. (D) IR image of exposure set up.

Calculation of Nanomaterial Heating Properties. The unfunctionalized NP heating data (Figure 24) and the NP solution properties (Table 3) were used for calculation of power generation from each sample under identical RF exposure conditions. The temperature after 70 s exposure was used for each sample to approximate the heat transfer rate in a linear region. The power generated per particle, per surface area, or per volume is presented in Table 4. A consistent trend is observed for power per volume for the Au NPs. The Ag NPs had approximately 2 orders of magnitude greater power per volume than either Au NP sample.

Table 4. Power Output Calculations With Respect to Number of Particles, Particle Surface Area, and Particle Volume.

Sample	Power / Particle (W/part.)	Power / Surface Area (W/nm²)	Power / Volume (W/nm³)
<i>Au 4 nm</i>	1.823E-14	3.626E-16	5.439E-16
<i>Au 13 nm</i>	5.459E-13	1.028E-15	4.746E-16
<i>Ag 10 nm</i>	5.435E-14	2.703E-14	2.027E-14

Discussion

Initial studies for heating of colloidal Au and Ag have been performed to assess NP heating under different conditions. It was first verified that any observed heating of the NPs, and therefore the solutions, was solely due to the NPs. To perform this verification, solutions of the metal salt precursors (HAuCl₄ and AgNO₃) and DI H₂O were tested. The NPs heated significantly more than the metal precursor solutions and water after 180 s (Figure 24).

To compare relative NP heating, the samples were diluted to equal particle volume concentrations. Two interesting phenomena were noticed when this was performed. First, in both Au NPs, the NPs dispersed in the NaCl solutions all heated more than the sample dispersed in water (Figure 25A and 25B). This heating was independent of NP functionalization since the unfunctionalized Au NPs in the NaCl solution heated nearly the same, leading to the conclusion that the NaCl was a contributing factor. Future studies will be performed to test NaCl solution without NPs. At low NP concentrations, it appears heating is enhanced by lower NaCl concentrations, provided the NPs are not aggregating. On the other hand, at high NP concentrations, it appears higher levels of NaCl in solution cause aggregation, which reduces heat transfer to the solution. Since the unfunctionalized NPs were observed to aggregate in the NaCl solution, it is hypothesized that the close proximity of the NPs causes a reduced effective surface area of the NPs which lessens heat transfer to the solution.

Second, the unfunctionalized Ag NP sample heated significantly more than the unfunctionalized Au NP samples at the same particle volume concentrations (Figure 25C). This indicates that the Ag NPs may respond more intensely to the RF exposure at this particular frequency. This was later confirmed when the calculations of the power output per particle / surface area / volume were performed. The W / nm³ for the 4 nm Au and 13 nm Au NPs were in the same order of magnitude, with only a 13 % difference, indicating that the RF heating is a volumetric effect (Table 4). Also, when adjusted to account for the lower concentration of the sample, the 8 nm Ag NPs showed at least a 42 fold increase in heating when compared to either Au NP sample (Table 4). This indicates that the heating effect is material dependent as well.

CONCLUSIONS AND FUTURE WORK

The future application of this project is to be able to use radio frequency (RF) exposure as a remote controlled, reversible “on / off” switch of NM-bound biomolecules (DNA, proteins, peptides, etc.) inside a biological environment. The specific aims of this project were to synthesize sub-10 nm Au and Ag colloids with minimal size distribution, functionalize with complimentary oligonucleotides for particle hybridization, examine biocompatibility, and determine the ability of RF signals to heat unfunctionalized and functionalized Au and Ag colloids. Each of these aims were independently attempted and accomplished in this study.

Due to their proven responsiveness to RF and their unique SPRs, Au and Ag colloids were chosen as the material for proof of concept in this study. The Au and Ag NPs provide easy visual feedback of changes in aggregation state through shifting of their SPR peak when in close proximity to another particle, causing a color shift of the solution which can also be tracked by UV-Vis. A facile, reproducible method was found to produce sub-10 nm Au and Ag colloidal NPs. The final sizes produced were an average of 4 nm for the Au colloid and 8 nm for the Ag colloid. 13 nm colloidal Au was also successfully reproduced from literature methods to provide a well-characterized sample for standardizing the following procedures.

The colloids were functionalized through simple attachment of thiol-modified biomolecules. Thiol-modified oligonucleotide sequences were chosen to functionalize the surface of the NPs since the oligonucleotides are very stable and have complementary sequences, allowing them to hybridize and form a network of particles. The hybridized oligonucleotides will dehybridize with increases of temperature, thereby decreasing particle aggregation, which can be tracked by DLS, and causing a visual color shift of the solution, which can be measured by UV-Vis. This provides instantaneous feedback of the particle state when exposed to an RF source. The NPs were successfully functionalized with oligonucleotides, successfully hybridized to form larger networks of particles, and successfully showed proper dehybridization of the oligonucleotides and release of the particles. The temperature at which the dehybridization occurred was characterized by examining the effect of varying solution salt concentrations and the presence of a PEG spacer between the binding sequence and the particle surface. The same color shift that occurs when the particles hybridized occurs in reverse when the particles dehybridize, providing another method to track particle status.

The biocompatibility and the ability of these particles to be taken into the cell were assessed as well. No significant adverse effects from the 4 nm Au or 8 nm Ag NPs were observed with either cell line tested. Uptake of both NPs was observed in both cell lines; however, it was only verified through TEM imaging of 4 nm Au NP treated cells with one cell line. Large aggregates of the 4 nm Au NPs were observed to be located in the cytoplasm of the cells, with some being contained in endosomes and some appearing to be located freely in the cytoplasm or locating around other cytoplasm structures. The functionalized and hybridized 13 nm Au NPs showed minimal influence to the overall cell viability as well, indicating that the functionalization did not have a specific effect on the cells. The hyperspectral imaging of the particles individually was used to provide a library resource so that once the functionalized and/or hybridized NPs were exposed to the cells, it could provide another method to track the status of the particles in the cellular environment pre-exposure, during exposure, and post-exposure.

The RF exposure of the NMs was successful, with some caveats. The experiments provided excellent initial characterization and verification of NP heating through RF exposure.

However, the RF system exposure setup was deemed to be very inefficient from the fact that similar heating of NPs in literature had occurred within 30 to 60 s of exposure at the same power output levels⁵³, whereas it took nearly 180 s to reach these heating levels. Some interesting observations were made as far as the dramatic reduction in heat transfer from the particle to the solutions once the particles were functionalized. A similar trend was seen with unfunctionalized NPs dispersed in the same salt solution. The calculation of the energy transfer to the solutions from the NPs verified the theory that this mechanism of heating by RF exposure is a material dependent property and is also dependent upon the volume of material present⁵⁰. However, there may be limitations to this effect such that once a certain size is reached; the effect reaches a limit similar to that seen in the bulk material⁵⁰.

Future work in the area of synthesis of NPs for this research will involve developing protocols to produce more exotic materials. These may consist of different shapes of the same materials such as rods or platelets, composite materials, or mixed material nano-structures to compare heating effects. Also, other methods of release of biomolecules may be explored, such as containing the biomolecule inside a hollow Au nanosphere to be released by heating of the materials until it structurally fails, similar to the materials produced in Gröger et al. (2009)⁷⁸. Functionalization of the NMs has limitless possibilities and purely depends upon the intended action of the NP-biomolecule conjugate. However, one near-term application is to control the action of a peptide in a cell signaling pathway by attaching the inhibitory peptide to the NP and modulating its ability to bind to its target through heating of the NP. As mentioned in the Biocompatibility Section (Section IV, page 58), the ERK peptide will be targeted in the PC-12 cells as to be able to control the cellular response, whether it is a proliferation or a differentiation response. Future biocompatibility studies will involve assessing any adverse effects of any new functionalization of the NPs as well as the general biocompatibility of any new materials synthesized. Assays will be used to also look for any adverse effects of RF exposure to the cells through DNA degradation, reactive oxygen species generation, and cell proliferation / viability assays. Most of the future work on this project will pertain to characterizing the RF interaction with the NMs. A large part of this characterization will be to look for unique absorption bands or spectra of RF using a low-power source and sweeping a range of frequencies from the high KHz to low GHz. Once optimal absorbance frequencies have been determined for each material, shape, etc; then a high-power RF source can be used to heat these materials more efficiently. Furthermore, studies will be conducted to address changes in the localized heating of functionalized NPs, as well as the effect of salt concentrations on the observed heating.

REFERENCES

1. The Royal Society (2004). Nanoscience and Nanotechnologies: Opportunities and Uncertainties. RS Policy document 19/04.
2. Royal Commission on Environmental Pollution (RCEP) (2008).
<http://www.independent.co.uk/news/science/the-big-question-what-is-nanotechnology-and-do-we-put-the-world-at-risk-by-adopting-it-1015518.html>
3. Kim, D., Zhang, Y., Voit, W., Rao, K., Kehr, J., Bjelke, B., Muhammed, M. (2001). Superparamagnetic Iron Oxide Nanoparticles for Bio-Medical Applications. *Scripta Mater.* 44, 1713-1717.
4. Murugan, R., Ramakrishna, S. (2005). Development of Nanocomposites for Bone Grafting. *Composites Sci. and Technol.* 65, 2385-2406.
5. Sinha, V., Trehan, A. (2003). Biodegradable Microspheres for Protein Delivery. *J. Controlled Release* 90, 261-280.
6. Wu, Y., Yang, W., Wang, C., Hu, J., Fu, S. (2005). Chitosan Nanoparticles as a Novel Delivery System for Ammonium Glycyrrhizinate. *Int. J. Pharmaceutics* 295, 235-245.
7. Chavany, C., Saison-Behmoaras, T., Le, D. T., Puisieux, F., Couvreur, P., Helene, C. (1994). Adsorption of oligonucleotides onto polyisohexylcyanoacrylate nanoparticles protects them against nucleases and increases their cellular uptake. *Pharm Res.* 11, 1370-1378.
8. Janes, K. A., Calvo, P., Alonso, M. J. (2001). Polysaccharide colloidal particles as delivery systems for macromolecules. *Adv Drug Deliv Rev.* 47, 83-97.
9. Moghimi, S. M., Hunter, A. C., Murray, J. C. (2001). Long-circulating and target-specific nanoparticles: theory to practice. *Pharmacol Rev.* 53, 283-318.
10. Panyam, J., Labhasetwar, V. (2003). Biodegradable nanoparticles for drug and gene delivery to cells and tissue. *Adv Drug Deliv Rev.* 55, 329-347.
11. Li, Z. Z., Wen, L. X., Shao, L., Chen, J. F. (2004). Fabrication of porous hollow silica nanoparticles and their applications in drug release control. *J Control Release.* 98, 245-254.
12. Kimbrell, G. (2006). Nanomaterials in Personal Care Products and FDA Regulation. The International Center for Technology Assessment. www.icta.org. 13 September 2006.
13. Ringer, S., Ratinac, K. (2004). On the role of characterization in the design of interfaces in nanoscale materials technology. *Microsc. Microanal.* 10, 324-335.

14. Chen, J., Wiley, B., Campbell, D., Saeki, F., Cang, L., Au, L., Lee, J., Li, X., Xia, Y. (2005). Gold Nanocages: Engineering Their Structure for Biomedical Applications. *Adv. Mater.* 17, 2255.
15. Hainfeld, J.F., Slatkin, D.N., Smilowitz, H.M. (2004). The use of gold nanoparticles to enhance radiotherapy in mice. *Phys. Med. Biol.* 49, 309-315.
16. Hirsch, L.R., Stafford, R.J., Bankson, J.A., Sershen, S.R., Rivera, B., Price, R.E., Hazle, J.D., Halas, N.J., West, J.L. (2003). Nanoshell-mediated near-infrared thermal therapy of tumors under magnetic resonance guidance. *Proc. Natl. Acad. Sci. U.S.A.* 100, 1549-1554.
17. Loo, C., Lin, A., Hirsch, L., Lee, M.H., Barton, J., Halas, N., West, J., Drezek, R. (2004). Nanoshell-enabled photonics-based imaging and therapy of cancer. *Technol. Cancer Res. Treat.* 3, 33-40.
18. Jadzinsky, P.D., Calero, G., Ackerson, C.J., Bushnell, D.A., Kornberg, R.D. (2007) Structure of a Thiol Monolayer-Protected Gold Nanoparticle at 1.1 Å Resolution. *Science*. 318 (5849), 430.
19. Whetten, R.L., Price, R.C. (2007) CHEMISTRY: Nano-Golden Order. *Science*. 318 (5849), 407.
20. Murphy, C.J., Gole, A.M., Stone, J.W., Sisco, P.N., Alkilany, A.M., Goldsmith, E.C., Baxter, S.C. (2008) Chemical sensing and imaging with metallic nanorods. *Chem. Commun.*, 544–557.
21. Shukla, R., Bansal, V., Chaudhary, M., Basu, A., Bhonde, R.R., Sastry, M. (2005) Biocompatibility of Gold Nanoparticles and Their Endocytotic Fate Inside the Cellular Compartment: A Microscopic Overview. *Langmuir*, 21, 10644-10654.
22. Li, J.J., Zou, L., Hartano, D., Ong, C.N., Bay, B.H., Yung, L. (2008) Gold Nanoparticles Induce Oxidative Damage in Lung Fibroblasts In Vitro. *Adv. Mater.* 20, 138-142
23. Pan, Y., Neuss, S., Leifert, A., Fischler, M., Wen, F., Simon, U., Schmid, G., Brandau, W., Jahnen-Dechent, W. (2007) Size-Dependent Cytotoxicity of Gold Nanoparticles. *Small*. 3 (11), 1941 – 1949.
24. Pernodet, N., Fang, X., Sun, Y., Bakhtina, A., Ramakrishnan, A., Sokolov, J., Ulman, A., Rafailovich, M. (2006) Adverse effects of citrate/gold nanoparticles on human dermal fibroblasts. *Small*. 2(6), 766-73.
25. Goodman, C.M., McCusker, C.D., Yilmaz, T., Rotello, V.M. (2004) Toxicity of gold nanoparticles functionalized with cationic and anionic side chains. *Bioconjug. Chem.* 15(4), 897-900.

26. Samuel, U., Guggenbichler, J. (2004) Prevention of catheter-related infections: the potential of a new nano-silver impregnated catheter. *Int. J. Antimicrob. Agents*. 23 Suppl 1, S75-8.
27. Percival, S., Bowler, P.G., Dolman, J. (2007) Antimicrobial activity of silver-containing dressings on wound microorganisms using an in vitro biofilm model. *Int. Wound J.* 4, 186-191.
28. Vigneshwaran, N., Kathe, A., Varadarajan, P., Nachane, R., Balasubramanya, R. (2007) Functional finishing of cotton fabrics using silver nanoparticles. *J. Nanosci. Nanotechnol.* 7, 1893-1897.
29. Cioffi, N., Ditaranto, N., Torsi, L., Picca, R., De Giglio, E., Sabbatini, L., Novello, L., Tantillo, G., Bleve-Zacheo, T., and Zambonin, P. (2005) Synthesis, analytical characterization and bioactivity of Ag and Cu nanoparticles embedded in poly-vinyl-methyl-ketone films. *Anal. Bioanal. Chem.* 382, 1912-1918.
30. Sun, R., Chen, R., Chung, N., Ho, C., Lin, C., Che, C. (2005) Silver nanoparticles fabricated in Hepes buffer exhibit cytoprotective activities toward HIV-1 infected cells. *Chem. Commun. (Camb)*. 5059-5061.
31. Kim, J., Kuk, E., Yu, K., Kim, J., Park, S., Lee, H., Kim, S., Park, Y., Park, Y., Hwang, C., Kim, Y., Lee, Y., Jeong, D., Cho, M. (2007) Antimicrobial effects of silver nanoparticles. *Nanomedicine*. 3, 95-101.
32. Elechiguerra, J.L., Burt, J., Morones, J., Camacho-Bragado, A., Gao, X., Lara, H., Yacaman, M. (2005) Interaction of silver nanoparticles with HIV-1. *J. Nanobiotechnology*. 3, 6.
33. Braydich-Stolle, L., Hussain, S., Schlager, J., Hofmann, M.C. (2005) In vitro cytotoxicity of nanoparticles in mammalian germ-line stem cells. *Toxicol. Sci.* 88, 412-419.
34. Carlson, C., Hussain, S., Schrand, A., Braydich-Stolle, L., Hess, K., Jones, R., Schlager, J. (2008) Unique Cellular Interaction of Silver Nanoparticles: Size-Dependent Generation of Reactive Oxygen Species. *J. Phys. Chem. B* 112 (43), 13608-13619
35. Su, X., Kanjanawarut, R. (2009) Control of Metal Nanoparticles Aggregation and Dispersion by PNA and PNA – DNA Complexes, and Its Application for Colorimetric DNA Detection. *ACS Nano*. 3(9), 2751–2759
36. Huang, K.-W., Yu, C.-J., Tseng, W.-L. (2010) Sensitivity enhancement in the colorimetric detection of lead (II) ion using gallic acid–capped gold nanoparticles: Improving size distribution and minimizing interparticle repulsion. *Biosensors and Bioelectronics*. 25, 984–989.
37. Li, L., Li, B., Qi, Y., Jin, Y. (2009) Label-free aptamer-based colorimetric detection of mercury ions in aqueous media using unmodified gold nanoparticles as colorimetric probe. *Anal. Bioanal. Chem.* 393:2051–2057.

38. Sugunan, A., Thanachayanont, C., Duttaa, J., Hilborn, J.G. (2005) Heavy-metal ion sensors using chitosan-capped gold nanoparticles. *Science and Technology of Advanced Materials*. 6,335–340.
39. Wang, Z., Lee, J., Lu, Yi. (2008) Label-Free Colorimetric Detection of Lead Ions with a Nanomolar Detection Limit and Tunable Dynamic Range by using Gold Nanoparticles and DNAzyme. *Adv. Mater.* 20, 3263–3267
40. Chah, S., Hammond, M., Zare, R. (2005) Gold Nanoparticles as a Colorimetric Sensor for Protein Conformational Changes. *Chemistry & Biology*, 12, 323–328
41. Mirkin, C., Letsinger, R., Mucic, R., Storhoff, J. (1996) A DNA-based method for assembling nanoparticles into macroscopic materials. *Nature*, 382:607-609.
42. Lee, J.-S., Seferos, D., Giljohann, D., Mirkin, C. (2008) Thermodynamically Controlled Separation of Polyvalent 2-nm Gold Nanoparticle-Oligonucleotide Conjugates. *J. Am. Chem. Soc.* 130, 5430–5431
43. Hurst, S., Hill, H., Mirkin, C. (2008) “Three-Dimensional Hybridization” with Polyvalent DNA-Gold Nanoparticle Conjugates. *J. Am. Chem. Soc.* 130, 12192–12200
44. Sebba, D., Lazarides, A. (2008(1)) Robust Detection of Plasmon Coupling in Core-Satellite Nanoassemblies Linked by DNA. *J. Phys. Chem. C* 112 (47), 18331-18339.
45. Sebba, D., LaBean, T., Lazarides, A. (2008(2)) Plasmon coupling in binary metal core–satellite assemblies. *Appl. Phys. B* 93: 69–78
46. Bernardi, P., Cavagnaro, M., Pisa, S., Piuze, E. (2003) Specific Absorption Rate and Temperature Elevation in a Subject Exposed in the Far-Field of Radio-Frequency Sources Operating in the 10–900-MHz Range. *IEEE Transactions on Biomedical Engineering*. 50(3):295-304
47. Curley, S., Cherukuri, P., Briggs, K., Patra, C., Upton, M., Dolson, E., Mukherjee, P. (2008) Noninvasive radiofrequency field-induced hyperthermic cytotoxicity in human cancer cells using cetuximab-targeted gold nanoparticles. *J. Experim. Therapeutics and Oncology*. 7:313-326
48. Cardinal, J., Klune, J., Chory, E., Jeyabalan, G., Kanzius, J., Nalesnik, M., Geller, D. (2008) Noninvasive radiofrequency ablation of cancer targeted by gold nanoparticles. *Surgery*. 144:125-132
49. Hamad-Schifferli, K., Schwartz, J., Santos, A., Zhang, S., Jacobson, J. (2002) Remote electronic control of DNA hybridization through inductive coupling to an attached metal nanocrystal antenna. *Nature*. 415:152-155.

50. Keblinski, P., Cahill, D., Bodapati, A., Sullivan, C., Taton, T.A. (2006) Limits of localized heating by electromagnetically excited nanoparticles. *J. Appl. Phys.* (2006) 100:054305.
51. Bendix, P., Nader, S., Reihani, S., Oddershede, L. (2010) Direct Measurements of Heating by Electromagnetically Trapped Gold Nanoparticles on Supported Lipid Bilayers. *ACS Nano*. 4(4), 2256-2262.
52. Gannon, C., Patra, C., Bhattacharya, R., Mukherjee, P., Curley, S. (2008) Intracellular gold nanoparticles enhance non-invasive radiofrequency thermal destruction of human gastrointestinal cancer cells. *J. Nanobiotech.* 6:2.
53. Moran, C., Wainerdi, S., Cherukuri, T., Kittrell, C., Wiley, B. Nicholas, N., Curley, S., Kanzius, J., Cherukuri, P. (2009) Size-Dependent Joule Heating of Gold Nanoparticles Using Capacitively Coupled Radiofrequency Fields. *Nano. Res.* 2: 400 405.
54. Wijaya, A., Schaffer, S., Pallares, I., Hamad-Schifferli, K. (2009) Selective Release of Multiple DNA Oligonucleotides from Gold Nanorods. *ACS Nano*. 3(1):80-86.
55. Kalambur, V., Longmire, E., Bischof, J. (2007) Cellular Level Loading and Heating of Superparamagnetic Iron Oxide Nanoparticles. *Langmuir*. 23(24): 12329-12336.
56. Pustovalov, V., Babenko, V. (2004) Optical properties of gold nanoparticles at laser radiation wavelengths for laser applications in nanotechnology and medicine. *Laser Phys. Lett.* 1(10):516–520.
57. Thanh, N., Rees, J., Rosenzweig, Z. (2002) Laser-based double beam absorption detection for aggregation immunoassays using gold nanoparticles. *Anal. Bioanal. Chem.* 374:1174–1178.
58. Bastus, N., Kogan, M., Amigo, R., Grillo-Bosch, D., Araya, E., Turiel, A., Labarta, A., Giral, E., Puentes, V. (2007) *Mater. Sci. and Eng. C*. 27:1236–1240.
59. Lacroix, L.-M., Carrey, J., Respaud, M. (2008) A frequency adjustable electromagnet for hyperthermia measurements on magnetic nanoparticles. *Review of Scientific Instruments*. 79:093909.
60. Turkevich, J., Stevenson, P., Hillier, J. (1953) The Formation of Colloidal Gold. *J. Phys. Chem.* 57(7), 670-673.
61. Frens, G. (1973) Controlled nucleation for the regulation of the particle size in monodisperse gold suspensions. *Nature Phys. Sci.* 241, 20-22.
62. Sutherland, W., Winefordner, J. (1992) Colloid filtration: a novel substrate preparation method for surface-enhanced Raman spectroscopy. *J. Colloid. Interface Sci.* 48

63. Grabar, K., Freeman, R., Hommer, M., Natan, M. (1995) Preparation and characterization of Au colloid monolayers. *Anal. Chem.* 67, 735-743.
64. Liang, Z., Zhang, J., Wang, L., Song, S., Fan, C., Li, G. (2007) A Centrifugation-based Method for Preparation of Gold Nanoparticles and its Application in Biodetection. *Int. J. Mol. Sci.* 8, 526-532.
65. DiScipio, R. (1996) Preparation of Colloidal Gold Particles of Various Sizes Using Sodium Borohydride and Sodium Cyanoborohydride. *Anal. Biochem.* 236, 168-170.
66. Obare, S., Hollowell, R., Murphy, C. (2002) Sensing strategy for Lithium ion based on gold nanoparticles. *Langmuir.* 18, 10407-10410.
67. Tom, R., Suryanarayanan, V., Reddy, P., Baskaran, S., Pradeep, T. (2004) Ciprofloxacin-protected gold nanoparticles. *Langmuir.* 20, 1909-1914.
68. Ding, Y., Zhang, X., Liu, X., Guob, R. (2006) Studies on interactions of thionine with gold nanoparticles. *Colloids and Surfaces A: Physicochem. Eng. Aspects.* 290, 82-88.
69. Lee, P., Meisel, D. (1982) Adsorption and surface-enhanced Raman of dyes on silver and gold sols. *Phys. Chem.* 86, 3391-3395.
70. Murdock, R., Braydich-Stolle, L., Schrand, A., Schlager, J., Hussain, S. (2008) Characterization of Nanomaterial Dispersion in Solution Prior to In Vitro Exposure via Dynamic Light Scattering. *Tox. Sci.* 101(2): 239-53
71. Haiss, W., Thanh, N., Aveyard, J., Fernig, D. (2007) Determination of Size and Concentration of Gold Nanoparticles from UV-Vis Spectra. *Anal. Chem.* 79, 4215-4221.
72. Liu, X., Atwater, M., Wang, J., Huo, Q. (2007) Extinction coefficient of gold nanoparticles with different sizes and different capping ligands. *Colloids and Surfaces B: Biointerfaces.* 58, 3-7.
73. Feldherr, C., Akin, D., Cohen, R. (2001) Regulation of functional nuclear pore size in fibroblasts. *J. Cell Sci.* 114(Pt 24): 4621-7.
74. Boukamp, P., Petrussevska, R., Breitkreutz, D., Hornung, J., Markham, A., Fusenig, N. (1988) Normal keratinization in a spontaneously immortalized aneuploid human keratinocyte cell line. *J. Cell Biol.* 761-771.
75. Greene, L., Tischler, A. (1976) Establishment of a noradrenergic clonal line of rat adrenal pheochromocytoma cells which respond to nerve growth factor. *Proc. Natl. Acad. Sci. USA* 73: 2424-2428.

76. Skebo, J., Grabinski, C., Schrand, A., Schlager, J., Hussain, S. (2007) Assessment of Metal Nanoparticle Agglomeration, Uptake, and Interaction Using High-Illuminating System. *International Journal of Toxicology*. 26(2), 135-141.
77. Schrand, A., Schlager, J., Dai, L., Hussain, S. (2010) Preparation of cells for assessing ultrastructural localization of nanoparticles with transmission electron microscopy. *Nat. Prot.* Published online 25 March 2010.
78. Gröger, H., Gyger, F., Leidinger, P., Zurmühl, C., Feldmann, C. (2009) Microemulsion Approach to Nanocontainers and Its Variability in Composition and Filling. *Adv. Mater.* 21, 1586–1590.

APPENDIX A

Example Calculation of Particle Characteristics

4 nm Au NP (Batch 5) Properties:

$$A = 1.4381 \text{ (O.D.)}$$

$$\varepsilon = 3.62E6 \text{ M}_{\text{particle}}^{-1} \text{cm}^{-1}$$

Molar Particle Concentration (Stock):

$$A = \varepsilon lc; 1.4381 = 3.62E6 * 1 \text{ cm} * c$$

$$c = \frac{1.4381}{3.62E6} = 3.973E-7 \text{ M}_{\text{particle}}$$

Number of Particles / Volume (Stock):

$$3.973E-7 \text{ M}_{\text{particle}} * \frac{6.022E23 \text{ particles}}{1 \text{ mole particles}} = 2.392E17 \frac{\text{Particles}}{L}$$

Total Particle Volume (Stock):

$$V = \frac{4}{3} \pi (2 \text{ nm})^3 * 2.392E17 \frac{\text{Particles}}{L} = 8.0157E18 \frac{\text{nm}^3}{L}$$

Solution Volume Necessary for 3E16 nm³/L Total Particle Volume:

$$V_s = \left(\frac{3E16 \text{ nm}^3 * 0.001}{8.0157E18 \frac{\text{nm}^3}{L}} \right) * \left(\frac{1 \mu L}{0.000001 L} \right) = 3.742 \mu L$$

Total Number Particles (3E16 nm³/L, 500 μL):

$$3.742 \mu L * \frac{0.000001 L}{1 \mu L} * 8.0157E18 \frac{\text{nm}^3}{L} = 8.952E11 \text{ Particles}$$

Total Particle Surface Area (3E16 nm³/L, 500 μL):

$$\frac{4}{3} \pi (2 \text{ nm})^3 * 4.500E13 \text{ Particles} = 4.500E13 \text{ nm}^2$$

APPENDIX B

Example Calculation of Particle Power Generation

4 nm Au NP (Batch 5) Properties:

$$T(t_0) = 20\text{ }^{\circ}\text{C} = 293\text{ K}$$

$$T(t_f) = 40\text{ }^{\circ}\text{C} = 313\text{ K}$$

$$t_f = 70\text{ seconds}$$

3.27E13 Au Particles, 500 μL Total Volume H_2O

Total Energy Change in Solution:

$$Q_T = mc \left(T(t_f) - T(t_0) \right)$$

$$Q_T = \left(500E - 3\text{ mL} * 0.9982 \frac{\text{g}}{\text{mL}} \right) * \left(4.1813 \frac{\text{J}}{\text{gK}} \right) * (313\text{ K} - 293\text{ K}) = 41.74\text{ J}$$

Total Power Generated:

$$\dot{Q}_T = \frac{Q}{\Delta t} = \frac{41.74\text{ J}}{70\text{ s}} = 0.596\text{ W}$$

Power Generated Per Particle Characteristic:

$$\dot{Q}_P = \frac{\dot{Q}_T}{\text{particles}} = \frac{0.596\text{ W}}{3.27E13\text{ particles}} = 1.823E - 14 \frac{\text{W}}{\text{particle}}$$

$$\dot{Q}_V = \frac{\dot{Q}_T}{V_P} = \frac{0.596\text{ W}}{33.510\text{ nm}^3} = 5.439E - 16 \frac{\text{W}}{\text{nm}^3}$$

$$\dot{Q}_{SA} = \frac{\dot{Q}_T}{SA_P} = \frac{0.596\text{ W}}{50.265\text{ nm}^2} = 3.626E - 16 \frac{\text{W}}{\text{nm}^2}$$

List of Acronyms, Abbreviations, and Symbols

μg	microgram
μL	microliter
Ag	silver
Au	gold
DLS	dynamic light scattering
DNA	deoxyribonucleic acid
FBS	fetal bovine serum
HaCaT	human keratinocyte cells
HSI	hyperspectral imaging
LDV	laser Doppler velocimetry
LSPR	local surface plasmon resonance
mg	milligram
mL	milliliter
MTS	methyl tetrazolium salt
mV	millivolt
MW	molecular weight
NM	nanomaterials
nm	nanometer
NP	nanoparticles
PBS	phosphate buffered saline
PC-12	rat pheochromocytoma cells
PdI	polydispersity index
PEG	polyethylene glycol
SD	standard deviation
SPR	surface plasmon resonance
TEM	transmission electron microscopy
UV-Vis	ultraviolet to visible absorption spectroscopy
W	Watt
Z-Ave	Z- average diameter